J. Fluid Mech. (1998), *vol.* 367, *pp.* 221–253. Printed in the United Kingdom

© 1998 Cambridge University Press

On the equation for spherical-particle motion: effect of Reynolds and acceleration numbers

By INCHUL KIM, SAID ELGHOBASHI
AND WILLIAM A. SIRIGNANO

Department of Mechanical and Aerospace Engineering, University of California,
Irvine, CA 92697, USA

(Received 31 May 1996 and in revised form 23 January 1998)

The existing model equations governing the accelerated motion of a spherical particle are examined and their predictions compared with the results of the numerical solution of the full Navier–Stokes equations for unsteady, axisymmetric flow around a *freely moving* sphere injected into an initially stationary or oscillating fluid. The comparison for the particle Reynolds number in the range of 2 to 150 and the particle to fluid density ratio in the range of 5 to 200 indicates that the existing equations deviate considerably from the Navier–Stokes equations. As a result, we propose a new equation for the particle motion and demonstrate its superiority to the existing equations over a range of Reynolds numbers (from 2 to 150) and particle to fluid density ratios (from 5 to 200). The history terms in the new equation account for the effects of large relative acceleration or deceleration of the particle and the initial relative velocity between the fluid and the particle. We also examine the temporal structure of the near wake of the unsteady, axisymmetric flow around a freely moving sphere injected into an initially stagnant fluid. As the sphere decelerates, the recirculation eddy size grows monotonically even though the instantaneous Reynolds number of the sphere decreases.

1. Introduction

Accurate prediction of particle (or droplet) dispersion is important in many turbulent two-phase flows such as spray combustion and atmospheric dispersion of pollutants. Since a general analytical solution of the Navier–Stokes equations for the unsteady three-dimensional flow around a sphere is not available, only a numerical solution of these equations can provide accurate information about the flow field. The forces on the particle can then be computed by integrating the normal and shear stresses around the particle, and Newton's law applied to obtain the acceleration of the particle. However, since these equations are unsteady and three-dimensional, they require excessive computing time. It is not possible to use this method to predict the simultaneous motion of many particles (order of 10^6 particles cm^{-3}) in a typical turbulent two-phase flow with the present and foreseeable computing capabilities.

Several equations accounting for the unsteadiness of the particle motion have been developed wherein a superposition of the steady drag and the unsteady (history) drag is used to obtain the forces on the particle. The available particle equations are reviewed next.

Basset (1888), Boussinesq (1903), and Oseen (1927) (hereinafter referred to as

BBO) studied the unsteady rectilinear motion of a sphere in a stagnant incompressible, viscous fluid. They solved the Navier–Stokes equations for a creeping flow by neglecting the advective acceleration terms and derived the following equation for the acceleration of the sphere:

$$m_p \frac{\mathrm{d}v}{\mathrm{d}t} = -6\pi a \mu_f v - \tfrac{1}{2} m_f \frac{\mathrm{d}v}{\mathrm{d}t} - 6a^2 (\pi \mu_f \rho_f)^{1/2} \int_0^t \frac{\mathrm{d}v/\mathrm{d}\tau}{(t-\tau)^{1/2}}\, \mathrm{d}\tau + (m_p - m_f) g, \tag{1.1}$$

where v is the sphere velocity, a is the sphere radius, m_p is the mass of the sphere, and m_f is the mass of the fluid displaced by the sphere.

Maxey & Riley (1983) re-derived from first principles the following equation for the motion of a sphere in a non-uniform creeping flow:

$$\begin{aligned} m_p \frac{\mathrm{d}\boldsymbol{v}}{\mathrm{d}t} = {} & 6\pi a \mu_f (\boldsymbol{u} - \boldsymbol{v}) + \tfrac{1}{2} m_f \frac{\mathrm{d}(\boldsymbol{u} - \boldsymbol{v})}{\mathrm{d}t} + m_f \frac{\mathrm{D}\boldsymbol{u}}{\mathrm{d}t} \\ & + 6a^2 (\pi \mu_f \rho_f)^{1/2} \int_0^t \frac{\mathrm{d}(\boldsymbol{u} - \boldsymbol{v})/\mathrm{d}\tau}{(t-\tau)^{1/2}}\, \mathrm{d}\tau + (m_p - m_f)\boldsymbol{g}, \end{aligned} \tag{1.2}$$

where the Faxén forces are not shown here, and $\boldsymbol{u}, \boldsymbol{v}$ are the velocity vectors of the carrier fluid and the sphere, respectively.

A widely used equation (e.g. Berlemont, Desjonqueres & Gouesbet 1990) for a noncreeping flow is obtained by empirically modifying the first right-hand side term in equation (1.2):

$$\begin{aligned} m_p \frac{\mathrm{d}\boldsymbol{v}}{\mathrm{d}t} = {} & \tfrac{1}{2} C_{Dstd} \pi a^2 \rho_f \mid \boldsymbol{u} - \boldsymbol{v} \mid (\boldsymbol{u} - \boldsymbol{v}) + \tfrac{1}{2} m_f \frac{\mathrm{d}(\boldsymbol{u} - \boldsymbol{v})}{\mathrm{d}t} + m_f \frac{\mathrm{D}\boldsymbol{u}}{\mathrm{d}t} \\ & + 6a^2 (\pi \mu_f \rho_f)^{1/2} \int_0^t \frac{\mathrm{d}(\boldsymbol{u} - \boldsymbol{v})/\mathrm{d}\tau}{(t-\tau)^{1/2}}\, \mathrm{d}\tau + (m_p - m_f)\boldsymbol{g}, \end{aligned} \tag{1.3}$$

where C_{Dstd} is the drag coefficient from the (steady) standard drag curve.

A simpler form of equation (1.3) is obtained by neglecting the second, third, and fourth terms on the right-hand side, resulting in

$$m_p \frac{\mathrm{d}\boldsymbol{v}}{\mathrm{d}t} = \tfrac{1}{2} C_{Dstd} \pi a^2 \rho_f \mid \boldsymbol{u} - \boldsymbol{v} \mid (\boldsymbol{u} - \boldsymbol{v}) + (m_p - m_f)\boldsymbol{g}. \tag{1.4}$$

Equation (1.4) is used in many practical engineering calculations assuming particles with large response time relative to the time scale of the flow. A detailed discussion of the conditions under which equation (1.4) is valid will be presented in § 3.2.

Odar & Hamilton (1964, hereinafter referred as to OH) and Odar (1966) studied experimentally the force on a guided sphere rectilinearly oscillating in an otherwise stagnant fluid for $0 \leqslant Re \leqslant 62$. They proposed an equation for the motion of a sphere with finite Reynolds number based on their experimental study as

$$m_p \frac{\mathrm{d}v}{\mathrm{d}t} = -\tfrac{1}{2} C_{Dstd} \pi a^2 \rho_f \mid v \mid v - C_a \tfrac{1}{2} m_f \frac{\mathrm{d}v}{\mathrm{d}t} - C_h\, 6a^2 (\pi \mu_f \rho_f)^{1/2} \int_0^t \frac{\mathrm{d}v/\mathrm{d}\tau}{(t-\tau)^{1/2}}\, \mathrm{d}\tau \tag{1.5}$$

with C_a and C_h obtained experimentally and given by

$$C_a = 2.1 - 0.132 M_{A1}^2/(1 + 0.12 M_{A1}^2),$$
$$C_h = 0.48 + 0.52 M_{A1}^3/(1 + M_{A1})^3,$$

where M_{A1} is the dimensionless relative acceleration defined by

$$M_{A1} = \frac{2a}{|\boldsymbol{u} - \boldsymbol{v}|^2} \left| \frac{\mathrm{d}|\boldsymbol{u} - \boldsymbol{v}|}{\mathrm{d}t} \right|. \tag{1.6}$$

M_{A1} is hereafter called the *acceleration number*. Note that $C_a \to 1$ and $C_h \to 1$ as $M_{A1} \to \infty$.

More recently, the numerical studies by Rivero, Magnaudet & Fabre (1991), Mei, Lawrence & Adrian (1991), and Chang & Maxey (1994, 1995) show that the added mass term for finite-Reynolds-number flows is the same as predicted by creeping flow and potential flow theory over a wide range of the dimensionless relative acceleration (i.e. C_a is unity).

Mei *et al.* (1991) studied an unsteady flow over a stationary sphere with small fluctuations in the free-stream velocity at finite Reynolds number ($0.1 \leqslant Re \leqslant 40$) using a finite-difference method and found that the Basset-force term in the equation of particle motion should have a kernel which must decay much faster than $(t-\tau)^{-1/2}$ at large time. Mei & Adrian (1992, hereinafter denoted as MA) and Mei (1994) considered the same problem as Mei *et al.* (1991) but for $Sl_\omega \ll Re \ll 1$ using a matched asymptotic expansion, where Sl_ω is the Strouhal number based on the angular frequency of the free stream and the sphere radius. They proposed a modified expression for the Basset force on the bases of the analytical result at small Reynolds number for low frequency, the numerical result at finite Reynolds number for low frequency, and the unsteady Stokes result for high frequency. Their proposed equation is

$$m_p \frac{\mathrm{d}v}{\mathrm{d}t} = \tfrac{1}{2} C_{Dstd} \pi a^2 \rho_f \mid u - v \mid (u - v) + \tfrac{1}{2} m_f \left(\frac{\mathrm{D}u}{\mathrm{D}t} - \frac{\mathrm{d}v}{\mathrm{d}t} \right) + m_f \frac{\mathrm{D}u}{\mathrm{D}t}$$
$$+ 6\pi\mu_f a \int_{-\infty}^{t} K(t-\tau, \tau) \frac{\mathrm{d}(u-v)}{\mathrm{d}\tau} \mathrm{d}\tau + (m_p - m_f) g \qquad (1.7a)$$

with the broad-frequency-range approximation for the integral kernel given by

$$K(t-\tau, \tau) = \left\{ \left[\frac{\pi (t-\tau) \nu_f}{a^2} \right]^{1/4} + \left[\frac{\pi}{2} \frac{|u(\tau) - v(\tau)|^3}{a \nu_f f_H^3(Re_t)} (t-\tau)^2 \right]^{1/2} \right\}^{-2}, \qquad (1.7b)$$

where $f_H(Re_t) = 0.75 + 0.105 Re_t(\tau)$; $Re_t = |u(\tau) - v(\tau)| 2a/\nu_f$. Now, equation (1.7*b*) shows that the history kernel decays initially as $t^{-1/2}$ but as t^{-2} at large time.

Maxey (1993) included the effect of the initial velocity difference between the sphere and the carrier fluid in the particle motion equation of Maxey and Riley (1983). The additional term is $6a^2(\pi\mu_f\rho_f)^{1/2}(u(0) - v(0))/t^{1/2}$.

Lovalenti & Brady (1993*a*, *b*) derived an expression for the hydrodynamic force acting on a rigid spherical particle translating with arbitrary time-dependent motion in an unsteady flow for small Reynolds number $Re < 1$. They also evaluated the corresponding expression for an arbitrary-shaped rigid particle for the case when the time scale of variation of the particle's slip velocity is much greater than the diffusive scale.

The next section provides a mathematical description of the flow considered, the governing equations, and the numerical solution procedure. In §3, the numerical solutions of the above equations are compared with those of the full Navier–Stokes equations for unsteady, axisymmetric flow around a freely moving sphere injected into an initially stationary or oscillating fluid, and a new equation for the arbitrary rectilinear particle motion is proposed. Section 4 provides a summary of the work. In the Appendix, it is shown that the proposed particle motion equation can predict the low-Reynolds-number ($Re < 1$) flow behaviour reasonably well even though our original emphasis was on the range $2 \leqslant Re \leqslant 150$.

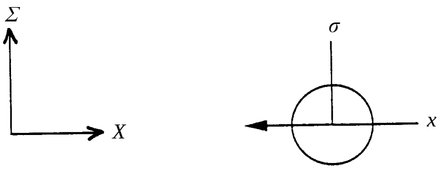

FIGURE 1. Flow geometry and coordinates: inertial cylindrical coordinates Σ, X; non-inertial cylindrical coordinates σ, x.

2. Problem statement and formulation

2.1. *Flow description*

Consider an unsteady, axisymmetric, incompressible, laminar flow generated by a spherical particle injected into a constant-property Newtonian fluid oscillating with time in the same direction as the particle motion direction shown in figure 1. The origin of a non-rotating non-inertial reference frame is chosen at the centre of the particle.

Three coordinate systems are used in our formulation: the inertial (fixed in space) cylindrical coordinates (X, Σ), the non-inertial cylindrical coordinates (x, σ), and the generalized coordinates (ξ, η). The origin of the coordinates (x, σ) coincides with the sphere centre. The coordinate ξ is in the radial direction and η is in the angular direction with respect to the sphere; they are used for the numerical solution of the Navier–Stokes equations. The generalized coordinate system can be easily adapted to two-dimensional or axisymmetric arbitrary geometries. See Kim, Elghobashi & Sirignano (1993, 1995).

The base flow in the far field varies with time in the X-direction and is expressed as

$$u_x(t) = f(t), \tag{2.1a}$$

$$u_\sigma(t) = 0. \tag{2.1b}$$

The associated far pressure field can be obtained from the Navier–Stokes equations as

$$p_b(x,t) = -\rho_f \frac{\mathrm{d}f}{\mathrm{d}t}(t)X + p_{ref}, \tag{2.2}$$

where p_{ref} is the reference pressure at $X = 0$. X is related to x as $X = x + X_p$, where X_p is the distance travelled by the particle and measured from the origin of the inertial coordinates (X, Σ).

2.2. *Governing equations and boundary conditions*

The momentum and continuity equations to be solved are

$$\nabla \cdot \boldsymbol{W} = 0, \tag{2.3a}$$

$$\rho_f \left(\frac{\mathrm{d}\boldsymbol{v}}{\mathrm{d}t} + \frac{\partial \boldsymbol{W}}{\partial t} + \nabla \cdot \boldsymbol{W}\boldsymbol{W} \right) = -\nabla p + \mu_f \nabla^2 \boldsymbol{W}, \tag{2.3b}$$

where $\boldsymbol{W}$ is the local disturbed fluid velocity vector relative to the sphere, v is the sphere velocity in the inertial reference system, and p is the local modified pressure discounting hydrostatic pressure variations.

The governing equations (2.3*a*) and (2.3*b*) are non-dimensionalized using the sphere radius a as the characteristic length and the initial injection velocity of the sphere

$v_o = v(0)$ as the characteristic velocity. The non-dimensional equations are cast in terms of the generalized coordinates (ξ, η) to treat an axisymmetric body of arbitrary shape. The numerical integration is performed using a cubic computational mesh with equal spacing ($\delta\xi = \delta\eta = 1$). In the present study, a spherical domain is used, and the grid reduces to an orthogonal, spherical grid. The grids are denser near the surface of the spherical particle, and the grid density in the radial direction is controlled by the stretching function developed by Vinokur (1983). The domain of the flow is bounded by $1 \leqslant \xi \leqslant N_1$, $1 \leqslant \eta \leqslant N_2$, where $\xi = 1$ and N_1 correspond, respectively, to the sphere surface and the far-field boundary surrounding the sphere; $\eta = 1$ and N_2 denote, respectively, the positive x-axis (downstream) and the negative x-axis (upstream).

The velocities on the sphere surface are zero due to the no-slip condition, and the pressure condition on the sphere is obtained from the momentum equation. The boundary conditions are

$$\frac{\partial p}{\partial n} = \mu_f \frac{\partial^2 W_n}{\partial n^2} - \rho_f \frac{\mathrm{d}v_n}{\mathrm{d}t}, \quad W_x = W_\sigma = 0 \quad \text{at} \quad \xi = 1, \tag{2.4a}$$

$$p = p_b, \; W_x = u_x - v, \; W_\sigma = 0 \quad \text{at} \quad \xi = N_1, \; N_{2m} \leqslant \eta \leqslant N_2, \tag{2.4b}$$

$$p = p_b, \; \frac{\partial W_x}{\partial x} = \frac{\partial W_\sigma}{\partial x} = 0 \quad \text{at} \quad \xi = N_1, \; 1 \leqslant \eta < N_{2m}, \tag{2.4c}$$

$$\frac{\partial p}{\partial \eta} = \frac{\partial W_x}{\partial \eta} = 0, \; W_\sigma = 0 \quad \text{at} \quad \eta = 1 \text{ and } N_2, \tag{2.4d}$$

where W_x and W_σ are the fluid velocities relative to the sphere in the x- and σ-directions, respectively, W_n is the fluid velocity relative to the sphere in the direction normal to the sphere surface, and v_n is the sphere velocity in the direction normal to the sphere surface; n denotes the direction normal to the sphere surface, $\partial/\partial n = (\xi_x^2 + \xi_\sigma^2)^{1/2}\partial/\partial\xi$, and $\eta = N_{2m}$ denotes the mid-plane between $\eta = 1$ and N_2.

In order to start the numerical solution of equations (2.3*a*) and (2.3*b*), the initial velocity field is obtained by superposing the initial velocities of the base flow and the sphere, and by imposing the no-slip condition on the sphere surface:

$$p_o = p_b, \quad W_{xo} = u_x(0) - v(0), \quad W_{\sigma o} = 0, \quad \text{except at} \quad \xi = 1, \tag{2.5a}$$

$$p_o = p_b, \quad W_{xo} = W_{\sigma o} = 0 \quad \text{at} \quad \xi = 1. \tag{2.5b}$$

The instantaneous acceleration of the sphere is obtained by applying Newton's second law and including the net buoyancy force:

$$m_p \frac{\mathrm{d}\boldsymbol{v}}{\mathrm{d}t} = (m_p - m_f)\boldsymbol{g} + \int_S \boldsymbol{T} \cdot \boldsymbol{n} \, \mathrm{d}S, \tag{2.6a}$$

where S is the surface of the sphere, and $\boldsymbol{T}$ is the fluid stress dyad and defined in tensor notation by

$$T_{ij} = -p\delta_{ij} + \tau_{ij} = -p\delta_{ij} + \mu\left(\frac{\partial W_i}{\partial x_j} + \frac{\partial W_j}{\partial x_i}\right). \tag{2.6b}$$

It should be noted that the net gravity force in equation (2.6*a*) is neglected in the all computations performed in the present paper since our objective is to study the surface forces.

The governing equations (2.3*a*), (2.3*b*), and (2.6*a*) along with the boundary and initial conditions are solved in an iterative manner to be explained in detail in the next subsection, § 2.3.

The drag force on the sphere is evaluated in dimensional form as

$$F_D = \int_S -p\boldsymbol{n}\cdot\boldsymbol{i}\,\mathrm{d}S + \int_S \boldsymbol{n}\cdot\boldsymbol{\tau}\cdot\boldsymbol{i}\,\mathrm{d}S, \tag{2.7}$$

where $\boldsymbol{\tau}$ is the viscous stress dyad which was defined in tensor form by equation (2.6*b*), and i is the unit vector in the X-direction. The non-dimensional drag coefficient is defined as

$$C_D = \frac{F_D}{\frac{1}{2}\rho_f \mid \boldsymbol{u}-\boldsymbol{v} \mid^2 \pi a^2}. \tag{2.8}$$

Note that u_x in equation (2.1*a*) will be denoted as u in the following sections.

2.3. *Numerical solution*

The three-dimensional numerical algorithm was developed to solve the Navier–Stokes equations in primitive form and described in Kim *et al.* (1993, 1995). Here, an axisymmetric, implicit, finite-difference algorithm has been developed to solve simultaneously the set of discretized partial differential equations. The method is based on an Alternating-Direction-Predictor-Corrector (ADPC) scheme to solve the time-dependent Navier–Stokes equations. ADPC is a slight variation of Alternating-Direction-Implicit (ADI) method and implemented easily when embedded in a large iteration scheme. The control volume formulation is used to develop the finite-difference equations from the governing equations with respect to the generalized coordinates (ξ, η). An important part of solving the Navier–Stokes equations in primitive variables is the calculation of the pressure field. In the present work, a pressure correction equation is employed to satisfy indirectly the continuity equation. The pressure correction equation is of the Poisson type and is solved by the Successive-Over-Relaxation (SOR) method.

The overall solution procedure is based on a cyclic series of guess-and-correct operations. The velocity components are first calculated from the momentum equations using the ADPC method, where the pressure field at the previous time step is employed. This estimate improves as the overall iteration continues. The pressure correction is calculated from the pressure correction equation using the SOR method, and new estimates for pressure and velocities are obtained. The change in sphere velocity is determined by computing the drag force on the sphere and applying Newton's second law. This process continues until the solution converges at each time step.

We now test the accuracy of the solution procedure by predicting the axisymmetric flow over a solid sphere.

Here we examine the flow generated by an impulsively started solid sphere in a quiescent fluid at two Reynolds numbers: 20 and 100. The time-dependent solution converges asymptotically to a steady state which is in good agreement with the available experimental data and correlations as shown in table 1. Table 1 lists the drag coefficient as a function of the computational grid density at Reynolds numbers 20 and 100 respectively, and compares them with the correlations of Clift, Grace & Weber (1978). Table 1 also shows the separation angle measured from the front

$N_1 \times N_2 \times N_3$	C_{DP}	C_{DV}	C_D	C_D^*	θ_s	θ_s^*
$Re = 20$						
21×21	1.087	1.789	2.876	—	166.3	—
31×31	1.057	1.759	2.816	—	172.6	—
41×41	1.042	1.733	2.775	—	180	—
51×51†	1.038	1.725	2.763	2.74	180	180
$Re = 100$						
21×21	0.558	0.590	1.148	—	124.1	—
31×31	0.533	0.581	1.114	—	125.6	—
41×41	0.524	0.580	1.104	—	126.2	—
51×51†	0.521	0.580	1.101	1.09	126.4	126.5
121×121‡	0.519	0.578	1.097	—	126.6	—

TABLE 1. Drag coefficient and separation angle as a function of grid density at $Re = 20$ and 100, where * denotes the data from the correlation of Clift *et al.* (1978) and Taneda (1956). † D21 domain; ‡ D121 domain.

stagnation point as a function of grid density at Reynolds number 20 and 100, in comparison with the data of Taneda (1956) and also with the correlations of Clift *et al.* (1978). The computations were performed with four different grids, $(N_1 \times N_2) = (21 \times 21)$, (31×31), (41×41), and (51×51) in a domain with an outer boundary located at 21 sphere radii from the sphere centre. The 51×51 grid domain with the outer boundary located at 21 sphere radii from the sphere centre will be referred to hereinafter as D21. The D21 domain with a non-dimensional time step of $\Delta t^* = 0.02$ was used in all the computations to be discussed in the paper except where stated otherwise.

We tested the accuracy of the solution procedure by varying the far-field boundary condition and the location of the outer boundary. In the first test, the far-field outflow boundary condition was changed from $\partial\phi/\partial x = 0$ ($\phi = V_x$ and V_σ) to $\partial\phi/\partial r = 0$. There was almost no effect on the drag coefficient and the near-wake size (the separation angle and length of the recirculation eddy) at Reynolds numbers 20 and 100. Our results show that separation does not occur at Reynolds number 20. In the second test, the location of the outer boundary of the computational domain in the downstream direction was increased from 21 to 121 sphere radii. This domain, with 121×121 grid points, is an ellipse-like region whose outer boundaries extend to 21 sphere radii in the upstream, top, and bottom directions of the sphere, and to 121 sphere radii in the downstream direction. This extended domain will be referred to hereinafter as D121. A computation with $Re = 100$ was performed with the extended domain to obtain the steady drag by relaxing a time-dependent Navier–Stokes solution to the steady state. The difference between the drag coefficient magnitudes from the computations with the D21 and D121 domains, normalized by the latter, is only 0.36% ($C_D = 1.097$ and 1.101 for the D21 and D121 domains, respectively). The drag coefficient and the separation angle from the computation with the D121 domain are included in table 1. Later, we will show in § 3.1 that our unsteady drag calculations are also independent of the domain size.

In the rest of this subsection, we present the numerical procedure that was employed to solve the equations of particle motion introduced in § 1.

The equation of particle motion is a first-order ordinary differential equation in time and is solved by employing the predictor-corrector method. The initial velocity difference term derived by Maxey (1993) has a $t^{-1/2}$ dependence, and the similar term in the equation to be proposed in § 3.2 is proportional to $t^{-1/2}$ as t approaches zero. While the force due to this term is infinity at $t = 0$, the effect on the sphere velocity due to this term is finite and integrable.

The history integral is singular at the upper limit. However, it can be integrated because of the square-root behaviour of the integrand when $\tau \to t$ and evaluated through the following expression given by Chung (1982) (see also Berezin & Zhidkov 1965):

$$\begin{aligned}\int_0^t \frac{\dot{U}}{f(t-\tau)}\mathrm{d}\tau &= \int_0^{n\Delta t} \frac{\dot{U}}{f(t-\tau)}\mathrm{d}\tau \\ &= \frac{\Delta t}{6}\sum_{i=1}^{n-1}\left[\frac{\dot{U}_{i-1}}{f(n\Delta t-(i-1)\Delta t)} + \frac{2(\dot{U}_{i-1}+\dot{U}_i)}{f(n\Delta t-(i-0.5)\Delta t)} + \frac{\dot{U}_i}{f(n\Delta t-i\Delta t)}\right] \\ &\quad + \frac{0.9\Delta t}{6}\left[\frac{\dot{U}_{n-1}}{f(\Delta t)} + \frac{2(\dot{U}_{n-1}+\dot{U}_n)}{f(0.55\Delta t)} + \frac{\dot{U}_n}{f(0.1\Delta t)}\right] \\ &\quad + \frac{0.1\Delta t}{2}\left[\frac{8\sqrt{2}}{3}\frac{\dot{U}_n}{f(0.05\Delta t)} - \frac{4}{3}\frac{\dot{U}_n}{f(0.1\Delta t)}\right] \qquad (2.9)\end{aligned}$$

where $\dot{U} \equiv \mathrm{d}(u-v)/\mathrm{d}\tau$, and $f(t-\tau) \sim (t-\tau)^{1/2}$ as $\tau \to t$.

It is noted that the negative sign of the coefficient 4/3 in the last term of equation (2.9) is typed incorrectly as positive in the paper by Chung (1982). It can be further noted that the published algorithm given by equation (2.9) does not give the exact result in the special test case where $\dot{U}(t)$ and $f(t)$ are each constant. Since the fractional error is less than $1/n$, this error is neglected.

3. Results and discussion

In § 3.1, we compare the solutions of the existing equations of particle motion (equations (1.3), (1.4), (1.5), and (1.7*a*)) with the Navier–Stokes solution. In § 3.2, we propose a new improved equation of particle motion and compare its solution with the Navier–Stokes solution.

3.1. *Comparison of the solution of the previous equations with that of the Navier–Stokes equations*

We now compare the numerical results of the equations (1.3), (1.4), (1.5), and (1.7*a*) introduced in § 1 with those from the full Navier–Stokes equations for unsteady, axisymmetric flow around a freely moving sphere injected into an initially stagnant fluid.

Figure 2(*a*) shows the drag coefficients of the sphere as a function of time ($0 \leqslant t^* \leqslant 200$) with initial particle Reynolds number $Re_{to} = 150$ and the sphere/fluid density ratio $\rho_r = 5$, where $t^* = tv_o/a = tv(0)/a$ and $Re_{to} = |u(0) - v(0)|2a/\nu_f$. The superscript $*$ denotes a dimensionless quantity hereinafter. At $t^* = 200$, the particle Reynolds number reduces to 4. The Basset history term in equations (1.3) and (1.5) causes too low a value for the drag coefficient compared with the Navier–Stokes solution. The drag coefficient from equation (1.7*a*) proposed by MA is the closest to that from the Navier–Stokes equations, but with increasing discrepancy as t^* increases. The drag coefficient from equation (1.7*a*) was computed excluding the negative time period ($-\infty < \tau < 0$) from the history integral. The effect of this negative time period will be discussed in § 3.2 and will be included in evaluating the history integral in §§ 3.3 and 3.4.

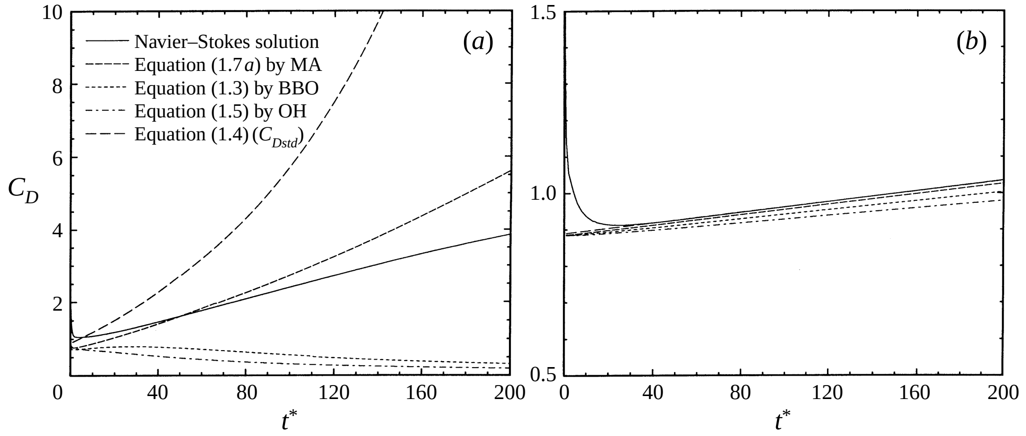

FIGURE 2. Drag coefficients as a function of time obtained from various equations for $Re_{to} = 150$ and (a) $\rho_r = 5$, (b) $\rho_r = 200$.

The accuracy of the Navier–Stokes solution shown in figure 2 (the most unsteady flow studied here) has been examined by using a much larger computational domain (denoted D121) with 121 × 121 grid points whose outer boundary was extended to 121 sphere radii in the downstream direction as described in § 2.3. We computed the drag coefficient of the sphere as a function of time ($0 \leqslant t^* \leqslant 200$) with the same parameters as those used in figure 2. The difference between the drag coefficient magnitudes obtained from the D21 and D121 domains, normalized by the latter, equals 0.77% at the final time $t_f = 200$ ($C_D = 3.86$ and 3.89 at the final time for the D21 and D121 domains, respectively). The maximum difference is 1% and occurs at $t = 5.2$, excluding the initial period following the sphere injection ($0 < t \leqslant 0.7$). Therefore, we concluded that the computational domain D21 whose outer boundary is located at 21 sphere radii from the sphere centre is large enough to compute the unsteady wake and drag correctly. Also, we computed the drag coefficient of the sphere as a function of time ($0 \leqslant t^* \leqslant 200$) with the time step reduced by half with the same parameters as those used in figure 2. The difference between the drag coefficient magnitudes from the two computations, normalized by the coefficient of the reduced time step, equals only 0.09% at $t_f = 200$.

Figure 2(b) shows the drag coefficients of the sphere as a function of time ($0 \leqslant t^* \leqslant 200$) with the same particle Reynolds number as in figure 2(a) but with the density ratio $\rho_r = 200$. At $t^* = 200$, the particle Reynolds number reduces to 109.8. The Basset history term in equations (1.3) and (1.5) still results in lower values for the drag coefficient. Now, the solution of equation (1.7a) gives a good approximation to that of the Navier–Stokes equations. However, it is noted that the solution of equation (1.4) also gives a good approximation and is very close to that of the Navier–Stokes equations. Thus, for high density ratio (ρ_r) the deviation from the Navier–Stokes solution is reduced. The effect of ρ_r will be explained in detail later in § 3.2

Lawrence & Mei (1995) show that a sudden acceleration of a particle creates an effective 'sink' that flows downstream in the particle wake. One might question the importance of keeping this sink within the computational domain in order to maintain numerical accuracy. The insertion of a moving particle at the initial time is equivalent to a sudden acceleration. The results of figure 2 show no indication of any abnormality in the solution at the time $t^* = 21$ when the sink should advect from the computational domain. Also there is no sensitivity of the solution to the size of the computational domain. We conclude that the hydrodynamic forces are adequately computed in the Reynolds number range of interest without attempts to track the sink behaviour far downstream.

3.2. *New equation for particle motion*

In order to understand the physics of the forces acting on the sphere, the momentum equation (2.3*b*) is non-dimensionalized using the sphere radius a as the characteristic length, the characteristic relative velocity of the sphere U_c, and the characteristic time scale t_c.

$$Sl\left(\frac{\mathrm{d}\boldsymbol{v}^*}{\mathrm{d}t'}+\frac{\partial \boldsymbol{W}^*}{\partial t'}\right)+\nabla\cdot\boldsymbol{W}^*\boldsymbol{W}^*=-\nabla p^*+\frac{2}{Re}\nabla^2\boldsymbol{W}^*, \tag{3.1}$$

where $Re = U_c 2a/\nu_f$, $Sl = (a/U_c)/t_c$, and $t' = t/t_c$. Strouhal number $Sl = (a/U_c)/t_c$ is the ratio of the time scale of residence a/U_c to that of the unsteadiness t_c (Lovalenti & Brady 1993*a*).

Equation (3.1) shows that when $Sl \gg 1$, the nonlinear term can be neglected with respect to the unsteady term. Under this condition the Basset (history) term accounts for the unsteady viscous force correctly. Otherwise, the nonlinear term cannot be neglected, and as a result, the Basset (history) term could not describe correctly the unsteady force and thus should be modified to include the effect of the nonlinear advection.

There are two typical cases where the magnitude of the Strouhal number may change: (i) oscillatory motion of the carrier fluid and (ii) non-inertial effect (i.e. acceleration or deceleration) of the sphere. The latter case may strongly depend on the sphere/fluid density ratio or the time elapsed after the release of a sphere from rest under gravity. Note that a high Strouhal number can occur in the latter case regardless of the magnitude of the flow oscillation.

MA found that the original integral kernel by Basset (the first right-hand side term in equation (1.7*b*) is valid only for high frequencies at low and finite Reynolds numbers. They modified the integral kernel by interpolating the term representing the original Basset kernel and the term representing low frequencies (the second right-hand side term in equation (1.7*b*)). However, the term representing low frequencies was developed by them under the assumption of small-amplitude oscillation of the free stream. Therefore, their modified kernel (1.7*b*) cannot correctly predict the behaviour of a spherical particle when it undergoes large acceleration or deceleration in a flow at low frequency. For example, as seen in the previous section, equation (1.7*a*) produces a less accurate solution for the drag of a sphere with lower density ratio than for the case with high density ratio; in other words, equation (1.7*a*) produces a less accurate solution for a sphere with higher deceleration than with lower deceleration.

The above analysis suggests that the term representing low frequencies should be weighted by the acceleration magnitude. We propose a weighting function that contains the time derivative of the relative velocity M_{A1} and the ratio ϕ_r of M_{A2} to M_{A1}. M_{A1} was defined by equation (1.6), and M_{A2} and ϕ_r are defined as follows:

$$M_{A2}(t)=\frac{(2a)^2}{|\boldsymbol{u}-\boldsymbol{v}|^3}\left|\frac{\mathrm{d}^2|\boldsymbol{u}-\boldsymbol{v}|}{\mathrm{d}t^2}\right| \quad ; \quad \phi_r(t)=\frac{M_{A2}}{M_{A1}}. \tag{3.2}$$

These dimensionless groups can be introduced through dimensional analysis to obtain the forces on the particle of unsteady motion (Clift *et al.* 1978).

Since there are many engineering applications in which particles (or droplets) are injected into the flow, e.g. gas-turbine and diesel engine combustion chambers, we must account for the initial relative velocity between the fluid and particle in the equation of particle motion. When a spherical particle is introduced suddenly into a flow, a vortex sheet is generated around the sphere due to the step change in the velocity across the sphere surface, and a high drag is produced initially on the sphere. Kim *et al.* (1995, 1996) showed the generation of the vortex sheet graphically and discussed the initial high drag in their study of unsteady flow interaction between a sphere and vortex tubes. The high drag is also shown in figure 2. As mentioned in § 1, Maxey (1993) derived a term representing the effect of the initial relative velocity between the particle and the carrier fluid. However this term is valid only for a creeping flow ($Re \to 0$) and should be modified for finite-Reynolds-number flows.

Based on the above discussion of the history integral kernel and the initial relative velocity, we propose a new equation for particle motion with the objective of removing the deficiencies of the existing equations. We begin with the following general form:

$$m_p \frac{\mathrm{d}v}{\mathrm{d}t} = \tfrac{1}{2} C_{Dstd} \pi a^2 \rho_f \mid u - v \mid (u - v) + \tfrac{1}{2} m_f \left(\frac{\mathrm{D}u}{\mathrm{D}t} - \frac{\mathrm{d}v}{\mathrm{d}t} \right) + m_f \frac{\mathrm{D}u}{\mathrm{D}t}$$

$$+6\pi\mu_f a \int_{-\infty}^{t} K(t-\tau,\tau) \frac{\mathrm{d}(u-v)}{\mathrm{d}\tau}\, \mathrm{d}\tau + (m_p - m_f) g. \tag{3.3}$$

The derivation of the history force is based on the condition that the particle is present at all times, and the lower limit of integration should be negative infinity. Now we show that the term associated with the initial velocity difference can be derived from the history integral with $-\infty$ lower limit:

$$\int_{-\infty}^{t} K(t-\tau,\tau) \frac{\mathrm{d}}{\mathrm{d}\tau} [u(\tau) - v(\tau)]\, \mathrm{d}\tau. \tag{3.4}$$

A particle instantaneously appearing in a fluid at $t = 0$ is the same as a particle being in a stagnant fluid for $-\infty < t < 0$ and having the bulk fluid velocity make a step change at $t = 0$. Thus, the relative velocity term in the history integral (3.4) can be rewritten as

$$[u(\tau) - v(\tau)]_{-\infty<\tau\leqslant t} = [u(0^+) - v(0^+)] H(\tau) - \left\{ [u(0^+) - v(0^+)] - [u(\tau) - v(\tau)] \right\}_{0<\tau\leqslant t}, \tag{3.5}$$

where $H(\tau)$ is the Heaviside step function and the term in the curly brace is assumed to be zero for $t < 0$. Equation (3.5) is differentiated with respect to τ to obtain

$$\left\{ \frac{\mathrm{d}}{\mathrm{d}\tau} [u(\tau) - v(\tau)] \right\}_{-\infty<\tau\leqslant t} = [u(0^+) - v(0^+)] \delta(\tau) + \left\{ \frac{\mathrm{d}}{\mathrm{d}\tau} (u(\tau) - v(\tau)) \right\}_{0<\tau\leqslant t}. \tag{3.6}$$

Substituting equation (3.6) into the history integral (3.4), we obtain

$$\int_{-\infty}^{t} K(t-\tau,\tau) \frac{\mathrm{d}(u-v)}{\mathrm{d}\tau}\, \mathrm{d}\tau = \int_{0^+}^{t} K(t-\tau,\tau) \frac{\mathrm{d}(u-v)}{\mathrm{d}\tau}\, \mathrm{d}\tau + K_1(t) [u(0^+) - v(0^+)], \tag{3.7}$$

where $K_1(t) \equiv K(t, 0)$. For the case where there is a steady flow prior to $t = 0$ with an impulse at $t = 0$, equation (3.7) is replaced by

$$\int_{-\infty}^{t} K(t-\tau,\tau) \frac{\mathrm{d}(u-v)}{\mathrm{d}\tau}\, \mathrm{d}\tau = \int_{0^+}^{t} K(t-\tau,\tau) \frac{\mathrm{d}(u-v)}{\mathrm{d}\tau}\, \mathrm{d}\tau$$

$$+K_1(t)\, [u(0^+) - v(0^+) - u(0^-) + v(0^-)]. \tag{3.8}$$

Now, equation (3.3) can be rewritten as

$$m_p \frac{\mathrm{d}v}{\mathrm{d}t} = \tfrac{1}{2} C_{Dstd} \pi a^2 \rho_f \mid u - v \mid (u - v) + \tfrac{1}{2} m_f \left(\frac{\mathrm{D}u}{\mathrm{D}t} - \frac{\mathrm{d}v}{\mathrm{d}t} \right) + m_f \frac{\mathrm{D}u}{\mathrm{D}t}$$
$$+ 6\pi\mu_f a \int_{0^+}^{t} K(t-\tau,\tau) \frac{\mathrm{d}(u-v)}{\mathrm{d}\tau}\, \mathrm{d}\tau + (m_p - m_f) g$$
$$+ 6\pi\mu_f a\, K_1(t)\, [u(0^+) - v(0^+) - u(0^-) + v(0^-)]. \qquad (3.9a)$$

We have used our numerical solution results to develop a form for the kernel $K(t-\tau,\tau)$ (and consequently for $K_1(t)$) that matches the low-Reynolds-number asymptotes at low and high frequencies. It also matches the Navier–Stokes equation solutions over wide ranges of frequency and Reynolds number. In particular, we have

$$K(t-\tau,\tau) = \left\{ \left[\frac{\pi(t-\tau)\nu_f}{a^2} \right]^{1/(2c_1)} + G(\tau) \left[\frac{\pi}{2} \frac{|u(\tau)-v(\tau)|^3}{a\nu_f f_H^3(Re_t)} (t-\tau)^2 \right]^{1/c_1} \right\}^{-c_1}, \qquad (3.9b)$$

$$G(\tau) = \frac{1}{1 + \beta (M_{A1}(\tau))^{1/2}}, \qquad (3.9c)$$

$$\beta = \frac{c_2}{1 + \phi_r \phi_r^{c_4} / [c_3(\phi_r + \phi_r^{c_4})]}, \qquad (3.9d)$$

$$f_H = 0.75 + c_5 Re_t(\tau), \qquad (3.9e)$$

where $Re_t = |u(\tau) - v(\tau)| 2a/\nu_f$.

Now, we show that the low-Reynolds-number asymptotes are correctly obtained with no dependence on the choice of c_1–c_5. Equation (3.9*c*) shows that as M_{A1} is reduced, $G(\tau)$ approaches unity, and the present kernel (equation (3.9*b*)) becomes similar in form to the kernel of equation (1.7*b*). On the other hand, as M_{A1} becomes large, $G(\tau)$ approaches zero, and the present kernel becomes of the same form as that of Basset (1888) (equation (1.1)). The β in the expression for $G(\tau)$ is not a constant but a function of ϕ_r, the ratio of M_{A2} to M_{A1}. This function behaves as follows: $\beta \simeq c_2(1 - \phi_r/c_3)$ for $\phi_r \ll 1$, and $\beta \simeq c_2 c_3/\phi_r^{c_4}$ for $\phi_r \gg 1$. Now we investigate the behaviour of the present kernel at high frequencies by normalizing the time by a characteristic frequency ω and the velocities by a characteristic velocity U_c, thus:

$$K(t'-\tau',\tau') = \left\{ \left[\frac{\pi(t'-\tau')}{Sl_\omega Re_R} \right]^{1/(2c_1)} + G(\tau') \left[\frac{\pi}{2} \frac{|u^*(\tau') - v^*(\tau')|^3}{f_H^3(Re_t)} \frac{Re_R}{Sl_\omega^2} (t'-\tau')^2 \right]^{1/c_1} \right\}^{-c_1},$$

where $\tau' = \tau\omega$ and $Re_R = U_c a/\nu_f$. Also, it can be shown that $G(\tau^*) \simeq Sl_\omega^{-0.4}$ as $Sl_\omega \gg 1$. Therefore, the present kernel becomes of the same form as that of Basset (1888) (equation (1.1)) as the dimensionless frequency becomes large.

It can be shown that the function $K_1(t)$ can be approximated as

$$K_1(t) = \left\{ \left[\frac{\pi t \nu_f}{a^2} \right]^{1/(2c_1)} + G_1 \left[\frac{\pi}{2} \frac{|u(0) - v(0)|^3}{a\nu_f f_H^3(Re_{to})} t^2 \right]^{1/c_1} \right\}^{-c_1}, \qquad (3.9f)$$

$$G_1 = \frac{1}{1 + c_6 Re_{to}^{-1/4} (\rho_r + 0.5)^{-1/2}}, \qquad (3.9g)$$

where $Re_{to} = |u(0) - v(0)| 2a/\nu_f$.

G_1 (equation (3.9g)) is obtained from $G(\tau = 0)$ (equation (3.9c)) as follows. From the equation of particle motion equation (3.9a), it can be shown that $\mathrm{d}v/\mathrm{d}t \simeq kt^{-1/2}$ as $t \to 0$, where $k = (4.5/a)(v_f/\pi)^{1/2}(\rho_r + 0.5)^{-1}(u(0) - v(0))$. Employing this form of $\mathrm{d}v/\mathrm{d}t$, the expressions for M_{A1}, M_{A2}, and ϕ_r as $t \to 0$ can be also derived. For example, ϕ_r is expressed by $\phi_r \simeq at^{-1}/(u(0) - v(0))$. Finally, $G(\tau \to 0)$ is obtained as

$$G(\tau \to 0) \sim \frac{1}{1 + \alpha\tau^{c_4 - 1/4} Re_{to}^{-1/4} (\rho_r + 0.5)^{-1/2}}$$

where $\alpha = c_2 c_3 (9\sqrt{2}/\pi^{1/2})^{1/2} (|u(0) - v(0)|/a)^{c_4 - 1/4}$. This equation shows that $G(0) = 0$ when $c_4 < 0.25$ but $G(0) = 1$ when $c_4 > 0.25$. However, the drag coefficient from the numerical computation of equation (3.9a) with $G_1 = G(0) = 0$ or $G_1 = G(0) = 1$ is too high or low for some initial period compared with that from the Navier–Stokes equations. Therefore, the constant c_4 is chosen as 0.25 so that $G(0)$ never equals 0 and does not equal 1 unless ρ_r becomes infinity. G_1 was introduced according to equation (3.9g) by following the form of $G(\tau \to 0)$, and the coefficient c_6 in the expression for G_1 is determined by numerical optimization. Note that for a fixed particle, G_1 becomes unity (equation (3.9g)), and thus the hydrodynamic force does not depend on the density of the particle. This fixed particle limit can be viewed as an infinite particle density limit. For a fixed particle, the left-hand side of equation (3.9a) should be replaced by the negative of the applied force required to fix the particle under the action of the hydrodynamic forces.

Equations (3.9f) and (3.9g) show that as the density ratio ρ_r becomes large, G_1 approaches unity, and the function $K_1(t)$ becomes proportional to $1/t^2$ at large time. This indicates that when ρ_r is large, the drag due to the initial velocity difference decays rapidly with time and becomes negligible compared to the quasi-steady drag C_{Dstd} in the new equation (3.9a). On the other hand, when ρ_r and the initial Reynolds number are both small, G_1 is small, and the $t^{-1/2}$ term in the function $K_1(t)$ remains important even at large time. This indicates that when the density ratio is small in low-Reynolds-number flows, the drag due to the initial velocity difference decays slowly with time and would not be negligible compared to the quasi-steady drag C_{Dstd} in the new equation at least for some finite time.

In order to calculate $K(t)$ from $K(t - \tau, \tau)$ at $\tau = 0$, the quantity $G(\tau)$ in the expression for $K(t - \tau, \tau)$ (equation (3.9b)) should be evaluated at $\tau = 0$. The notation $G(\tau = 0) = G_1$ is used. Now equation (3.7) or (3.8) is a more convenient form than equation (3.4) since the initial relative velocity appears explicitly. It should be noted that the representation of the effect of the initial relative velocity in equation (3.9a) differs from the representation in Maxey's (1993) formulation through the addition of the second term on the right in equation (3.9f). The difference becomes important at lower acceleration magnitudes.

The value of the constant c_4 was determined as 0.25 before when $G(\tau \to 0)$ was evaluated. The values of the other five constants c_i ($i = 1, 2, 3, 5, 6$) in the above equations are determined by comparing the numerical solutions of equation (3.9a) with those of the Navier–Stokes equations. The six constants are

$$c_1 = 2.5, \quad c_2 = 22.0, \quad c_3 = 0.07, \quad c_4 = 0.25, \quad c_5 = 0.126, \quad c_6 = 17.8\,. \qquad (3.9h)$$

Some features of equation (3.9a) are discussed in the following.

When $G(\tau)$ equals unity, the present integral kernel (equation (3.9b)) is similar to equation (1.7b) by MA, but with values of c_1 and c_5 different from those used in equation (1.7*b*). MA used the values 2 and 0.105 for c_1 and c_5 which were determined respectively by an interpolation and curve fitting.

Equation (3.9*a*) has not been tested for non-uniform free streams. It might fail when the characteristic length for variation in the free stream becomes as small as or smaller than the particle dimension.

Lawrence & Mei (1995) investigated the long-time behaviour of the drag on a body in impulsive motion by solving a special case of a step change in the fluid velocity from U_1 to U_2 (both U_1 and U_2 are constant) in a flow past a body fixed in space. Lovalenti & Brady (1995) also used the same special case to compare their results with those obtained by Lawrence & Mei (1995) for small Reynolds number ($Re \leqslant 1$). Our proposed expression for the history force has the same form as that proposed by MA for that special case as discussed next.

For the case of $U_1 = 0$ and $U_2 \neq 0$, which implies that the fluid velocity is changed from 0 to U_2 at $t = 0$ while the sphere is fixed in space, the history integral with zero lower limit in equation (3.9*a*) is zero because U_2 is constant and thus the relative acceleration is zero. But the initial relative velocity term is non-zero and equals $U_2K(t)$ which is identical to the history integral of MA, because ρ_r in our equation (3.9*g*) equals ∞ for a sphere fixed in space and G_1 becomes unity.

For the case of $U_1 \neq 0$ and $U_2 \neq 0$, which implies that the fluid velocity is changed from U_1 to U_2 at $t = t_1$ while the sphere is fixed in space, the initial relative velocity term is zero. But the history integral with zero lower limit in equation (3.9*a*) is non-zero and equals $(U_2 - U_1)K(t)$ which is identical to the history integral of Mei & Adrian (1992) for the same reason as above.

3.3. *Comparison of the solution of the proposed equations with the Navier–Stokes solution for an initially stagnant flow*

Figure 3(*a*) shows the drag coefficients of the sphere as a function of time for the same conditions as in figure 2(*a*), but here the drag coefficient from the new equation (3.9*a*) is compared with those from the BBO equation (1.3) and equation (1.7*a*) by MA including an initial velocity difference term. We note that the initial velocity difference terms are different among the equations because the integral kernels are different among them. The initial velocity difference term added to the BBO equation (equation (1.3)) is the term given by Maxey (1993) and discussed earlier in § 1. The initial velocity difference term added to equation (1.7*a*) is the term given by setting $G_1 = 1$ with $c_1 = 2$ and $c_5 = 0.105$ in equations (3.9*f*) and (3.9*e*). It is shown in figure 3(*a*) that our new equation (3.9*a*) gives the most accurate solution.

Comparing figures 2(*a*) and 3(*a*), we see that the initial velocity difference term with $t^{-1/2}$ improves equation (1.3). However, the appropriate decay of this term is t^{-2} for finite initial particle Reynolds number (see equation (3.9*f*)). Note that the initial velocity difference term decays as $t^{-1/2}$ when $Re_{to} \ll 1$ in a creeping flow (see equations (3.9*g*) and (3.9*f*)).

Figure 3(*b*) shows the drag coefficients as a function of time ($0 \leqslant t^* \leqslant 100$) for the same conditions as in figure 3(*a*) except that $Re_{to} = 75$. At $t^* = 100$, the particle Reynolds number equals 2.98. Figure 3(*c*) displays the drag coefficients as a function of time ($0 \leqslant t^* \leqslant 50$) for the same conditions as in figure 3(*a*) except that $Re_{to} = 38$. At $t^* = 50$, the particle Reynolds number equals 2.18. It is seen that the new equation (3.9*a*) gives the best solution for low initial particle Reynolds numbers as well.

In order to examine the contributions to the total drag coefficient from each term

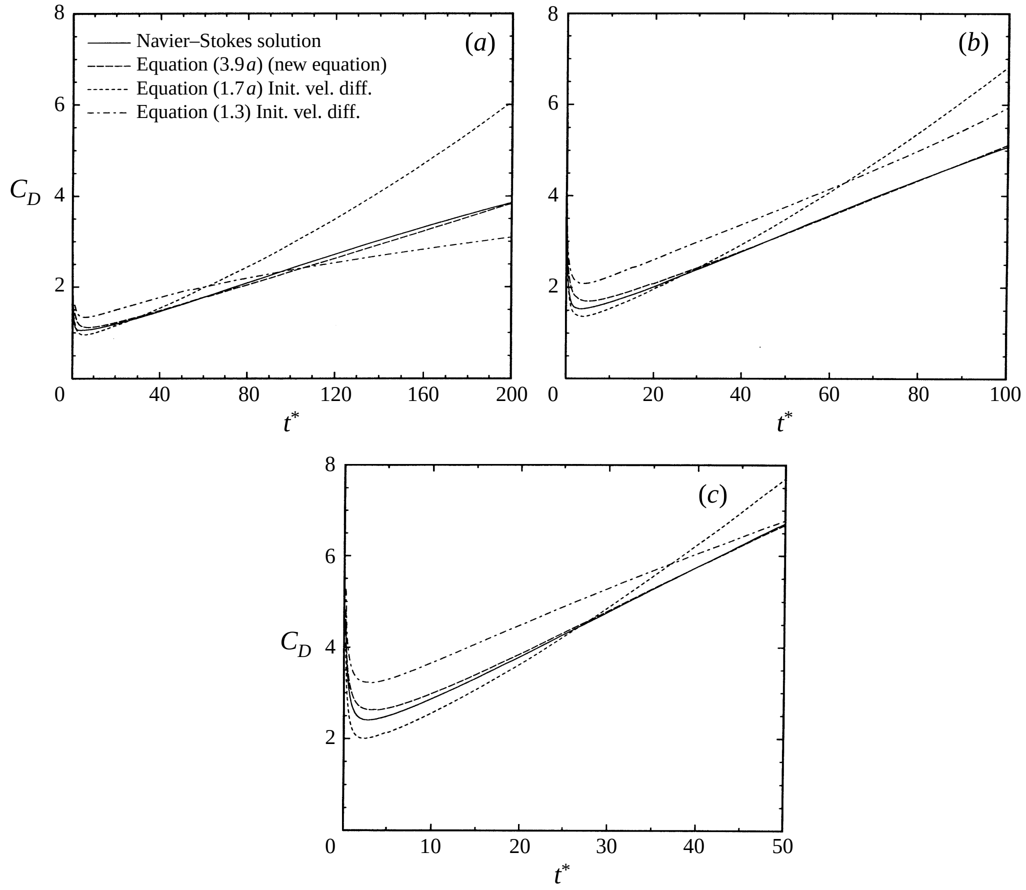

FIGURE 3. Drag coefficients as a function of time obtained from various equations with an initial velocity difference term for $\rho_r = 5$ and (a) $Re_{to} = 150$, (b) $Re_{to} = 75$, (c) $Re_{to} = 38$.

on the right-hand side of (3.9a), we may rewrite (3.9a) as

$$\begin{aligned} m_p \frac{\mathrm{d}v}{\mathrm{d}t} &= \tfrac{1}{2}\pi a^2 \rho_f \mid u - v \mid (u - v)\, C_{Dtot} \\ &= \tfrac{1}{2}\pi a^2 \rho_f \mid u - v \mid (u - v)(C_{Dstd} + C_{Dadd} + C_{Dfld} + C_{Dhis} + C_{Dini} + C_{Dgrv}) \quad (3.10) \end{aligned}$$

where C_{Dstd} represents the quasi-steady drag coefficient from the (steady) standard drag curve, C_{Dadd} represents the drag coefficient due to the added mass force, C_{Dfld} represents the drag coefficient due to the carrier fluid acceleration or the gradient of the pressure and the shear stress at the position of the sphere, C_{Dhis} represents the drag coefficient due to the (unsteady) history force which is the integral of the past relative acceleration of the sphere weighted by the kernel K; C_{Dini} represents the drag coefficient due to the initial velocity difference between the carrier fluid and the sphere, and C_{Dgrv} represents the drag coefficient due to the net gravity force which equals zero in the present simulations.

Figure 4(a) shows C_{Dtot}, C_{Dstd}, C_{Dadd}, C_{Dhis}, and C_{Dini} as a function of time. They are obtained from the new equation for initial particle Reynolds number $Re_{to} = 150$ and the sphere/fluid density ratio $\rho_r = 5$ (the same parameters as used in figure 3(a)). The drag coefficient due to the history integral is large compared to that in the case

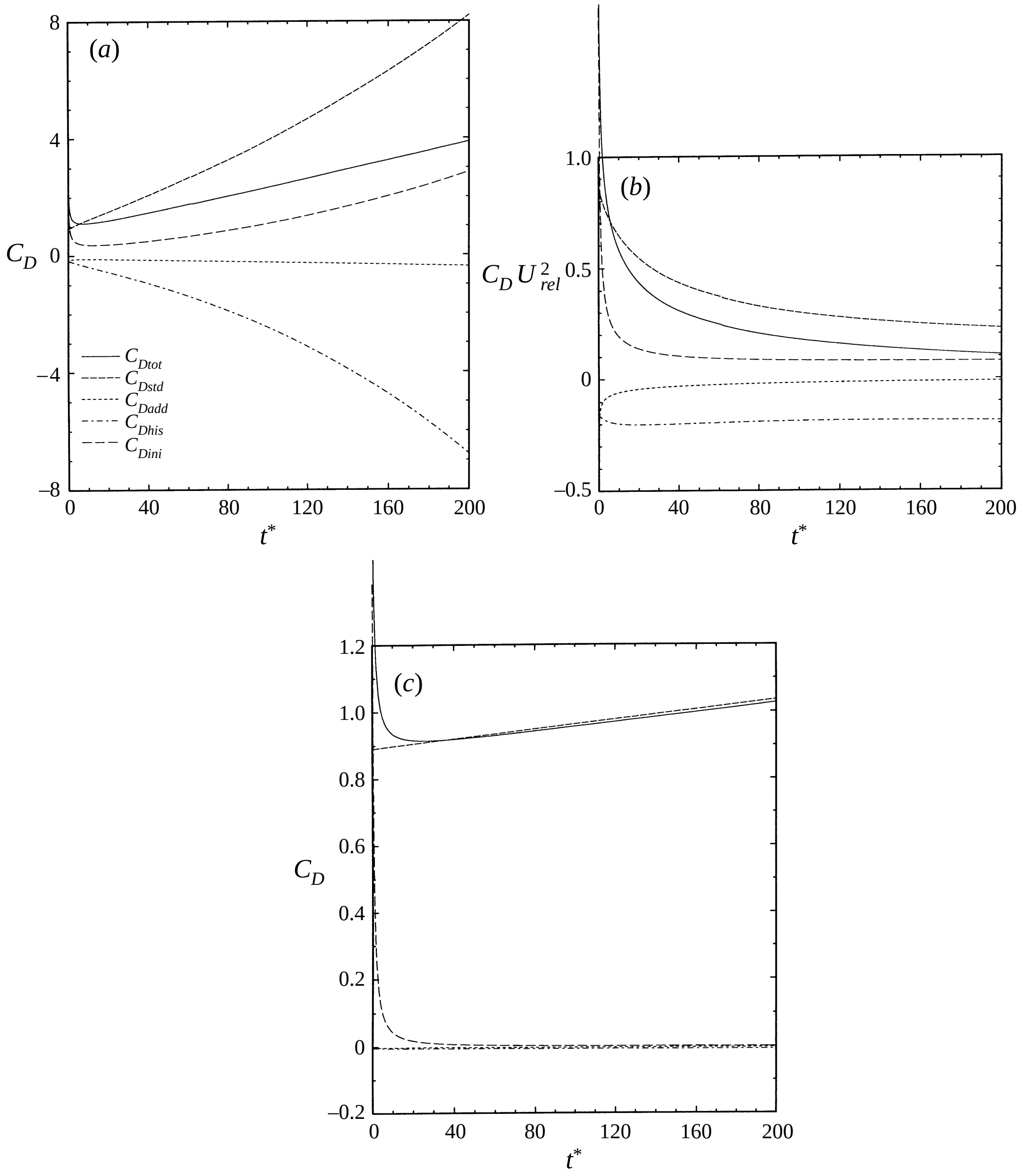

FIGURE 4. (*a*) C_{Dtot}, C_{Dstd}, C_{Dadd}, C_{Dhis}, and C_{Dini} as a function of time obtained from the new equation for $Re_{to} = 150$ and $\rho_r = 5$. (*b*) As (*a*) but the drag coefficients are multiplied by U^2_{rel}. (*c*) As (*a*) but for $\rho_r = 200$.

of $\rho_r = 200$ as shown in figure 4(*c*) because the sphere experiences high deceleration. Note that the drag coefficient due to the initial velocity difference increases slowly with time. The reason is that the drag coefficient is obtained by normalizing the force with the instantaneous relative velocity (see equation (2.8)) and the magnitude of the relative velocity decays rapidly as will be seen in figure 6(*b*). Figure 4(*b*) shows the temporal behaviour of the same drag coefficients as in figure 4(*a*) multiplied by U^2_{rel}, where $U_{rel} = |u - v|/v_o$, and thus represents the actual forces on the sphere. In this

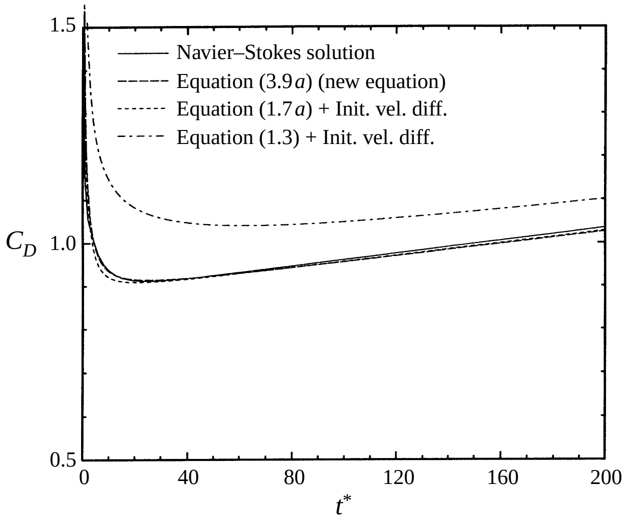

FIGURE 5. Drag coefficients as a function of time obtained from various equations with an initial velocity difference term for $Re_{to} = 150$ and $\rho_r = 200$.

case of a decelerating particle, the history term provides a negative contribution. The effect of acceleration with an oscillatory flow is considered later.

Figure 5 compares the drag coefficients as a function of time, for the same conditions as in figure 2(*b*), computed from the new equation (3.9*a*) and those from (1.3) and (1.7*a*) including an initial velocity difference term. Solutions from both (1.7*a*) and (3.9*a*) agree well with that of the Navier–Stokes equations. As mentioned in the discussion of figure 3(*a*), the initial velocity difference terms are different among the equations because the integral kernels are different. By comparing the results from equation (1.3) in figure 2(*b*) (which does not account for the initial velocity difference) and figure 5, we now see that the initial velocity difference term with $t^{-1/2}$ derived by Maxey (1993) for a creeping flow is not appropriate for the case of finite-Reynolds-number flows.

The improved performance of equation (1.7*a*) for the case of higher density ratio is due to the small acceleration number M_{A1} in the case of higher density ratio as will be shown in figure 6(*a*). When M_{A1} is small, the function $G(\tau)$ in (3.9*b*) approaches unity, and thus the integral kernel of (3.9*a*) approaches that of (1.7*a*).

Figure 4(*c*) displays the contributions to the total drag coefficient from C_{Dstd}, C_{Dadd}, C_{Dhis}, and C_{Dini} which are obtained with the new equation for initial particle Reynolds number $Re_{to} = 150$ and the sphere/fluid density ratio $\rho_r = 200$. It is observed that the contributions from C_{Dadd}, C_{Dhis}, and C_{Dini} are small except for the large C_{Dini} for a short initial period, and that the quasi-steady drag coefficient approximates the total drag coefficient very well. The force due to the initial velocity difference is small due to the high density ratio as mentioned earlier.

Figure 6(*a*) shows the acceleration number M_{A1} as a function of time for four different cases: (i) $\rho_r = 5$ and $Re_{to} = 38$, (ii) $\rho_r = 5$ and $Re_{to} = 75$, (iii) $\rho_r = 5$ and $Re_{to} = 150$, and (iv) $\rho_r = 200$ and $Re_{to} = 150$. It is seen that $M_{A1}(t)$ is very small for the case of $\rho_r = 200$ and $Re_{to} = 150$, and figure 4(*c*) showed that the history force is very small for that case as well. Furthermore, figures 4(*a*) and 6(*a*) indicate that the history force is not small when $M_{A1}(t)$ is not small. This indicates that M_{A1} controls

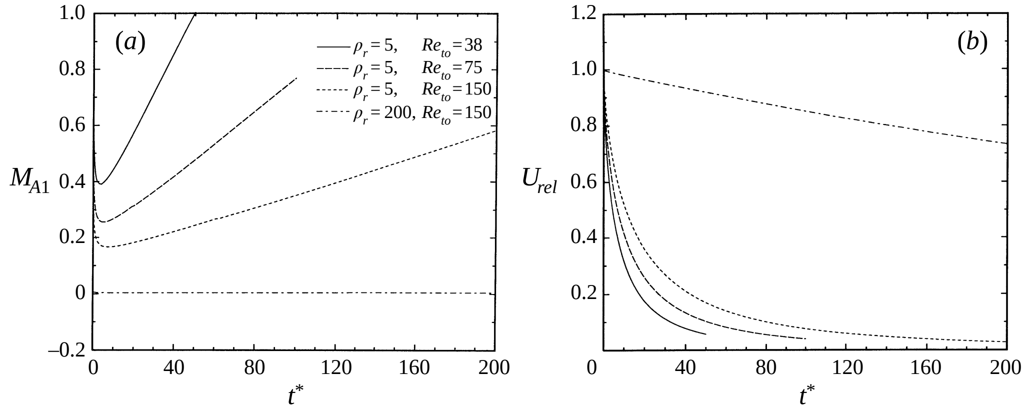

FIGURE 6. (*a*) Dimensionless relative acceleration M_{A1} and (*b*) dimensionless relative velocity U_{rel} as a function of time for four different cases.

the magnitude of the history integral which will be discussed in more detail later in this section.

Figure 6(*b*) portrays the dimensionless relative velocity $U_{rel} = |u - v|/v_o$ as a function of time for the same cases as in figure 6(*a*). This figure indicates that the lower the density ratio the higher is the deceleration, and the lower the initial Reynolds number the higher is the deceleration.

3.4. *Comparison of the solution of the proposed equations with the Navier–Stokes solution for an oscillating flow*

Now we compare the numerical results of the new equation (3.9*a*) and the equations (1.4), (1.5), and (1.7*a*) introduced in § 1 with those from the full Navier–Stokes equations for unsteady, axisymmetric flow around a freely moving sphere injected into a fluid oscillating with time in the X-direction as

$$u_x(t) = \alpha_1 |v| \sin \omega t, \tag{3.11a}$$

$$u_\sigma(t) = 0, \tag{3.11b}$$

where α_1 is a constant controlling the amplitude and ω is the angular frequency. The associated far pressure field can be obtained from the Navier–Stokes equations as

$$p_b(x,t) = -\rho_f \alpha_1 \left(\frac{\mathrm{d}|v|}{\mathrm{d}t} \sin \omega t + |v| \omega \cos \omega t \right) X + p_{ref} \tag{3.12}$$

where p_{ref} is the reference pressure at $X = 0$.

Figure 7 shows the drag coefficients of the sphere as a function of time ($0 \leqslant t^* \leqslant 200$) for $Re_{to} = 150$ and $\rho_r = 5$ with the base flow oscillating with $Sl_\omega = 0.1$ and $\alpha_1 = 0.02$. This figure compares the drag coefficients obtained from the solution of Navier–Stokes equations, the new equation (3.9*a*), equation (1.7*a*) by MA including an initial velocity difference term, equation (1.5) by OH, and equation (1.4) with only C_{Dstd}. It is shown that equation (1.7*a*) with an initial velocity difference term produces higher drag coefficients (except for some initial period) than do the Navier–Stokes equations. Again, the new equation (3.9*a*) produces very good agreement with the Navier–Stokes equations.

Figure 8 shows the temporal behaviour of C_{Dtot}, C_{Dstd}, C_{Dadd}, C_{Dhis}, C_{Dini}, and C_{Dfld} obtained from the new equation for the same conditions used in figure 7. The drag

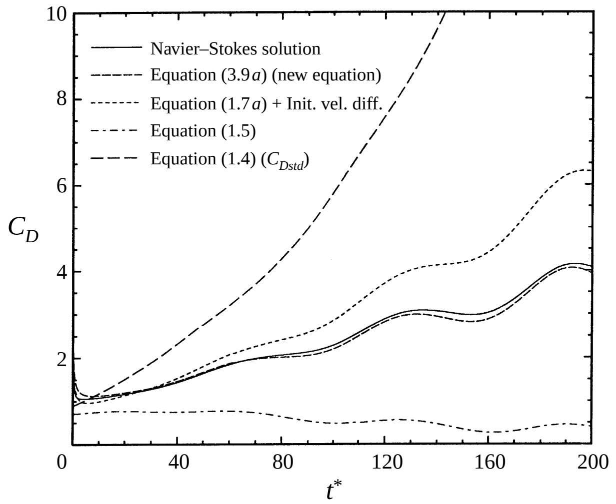

FIGURE 7. Drag coefficients as a function of time obtained from various equations for $Re_{to} = 150$ and $\rho_r = 5$ with the base flow oscillating with $Sl_\omega = 0.1$ and $\alpha_1 = 0.02$.

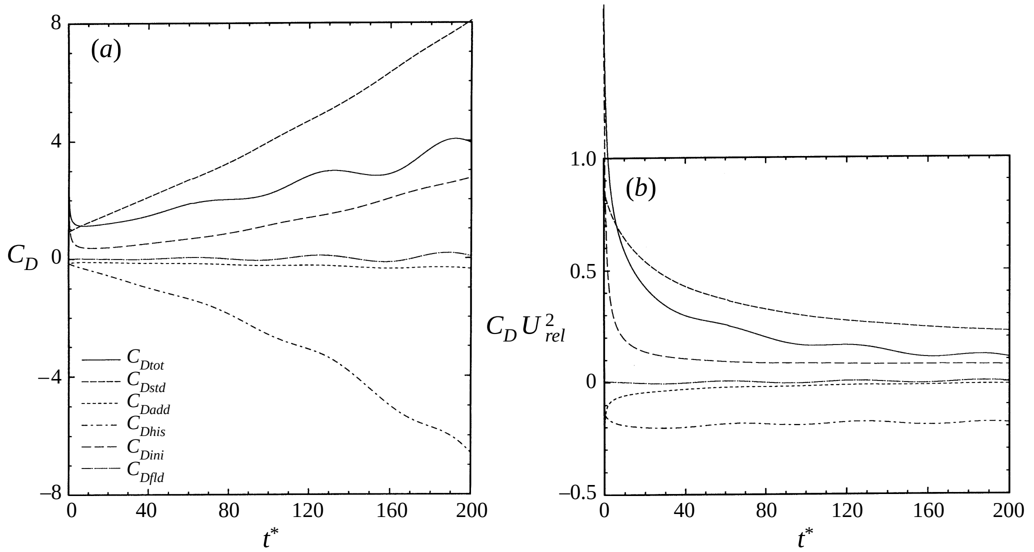

FIGURE 8. (*a*) C_{Dtot}, C_{Dstd}, C_{Dadd}, C_{Dhis}, C_{Dini}, and C_{Dfld} as a function of time obtained from the new equation for the same parameters as used in figure 7. (*b*) As (*a*) but the drag coefficients are multiplied by U^2_{rel}.

coefficient due to the history integral is large compared with that in the case of $\rho_r = 200$ as shown in figure 12 because the sphere experiences high deceleration. The magnitude of the relative velocity U_{rel} decays rapidly as will be seen in figure 17(*b*). Figure 8(*b*) presents the temporal behaviour of the same drag coefficients as in figure 8(*a*) multiplied by U^2_{rel} and thus represents the actual forces on the sphere.

Figure 9 displays the drag coefficients of the sphere as a function of time ($0 \leqslant t^* \leqslant 200$) for the same conditions as used in figure 7 except $Sl_\omega = 0.4$ It is seen that equation (1.7*a*) with an initial velocity difference term produces higher drag coefficients (except for some initial period) than do the Navier–Stokes equations.

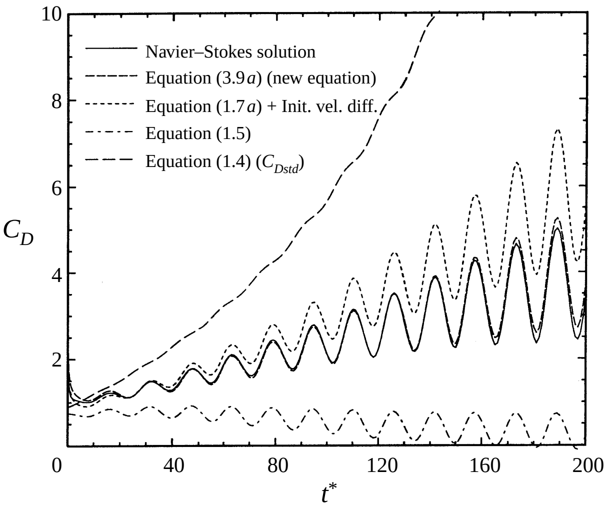

FIGURE 9. Drag coefficients as a function of time obtained from various equations for $Re_{to} = 150$ and $\rho_r = 5$ with the base flow oscillating with $Sl_\omega = 0.4$ and $\alpha_1 = 0.02$.

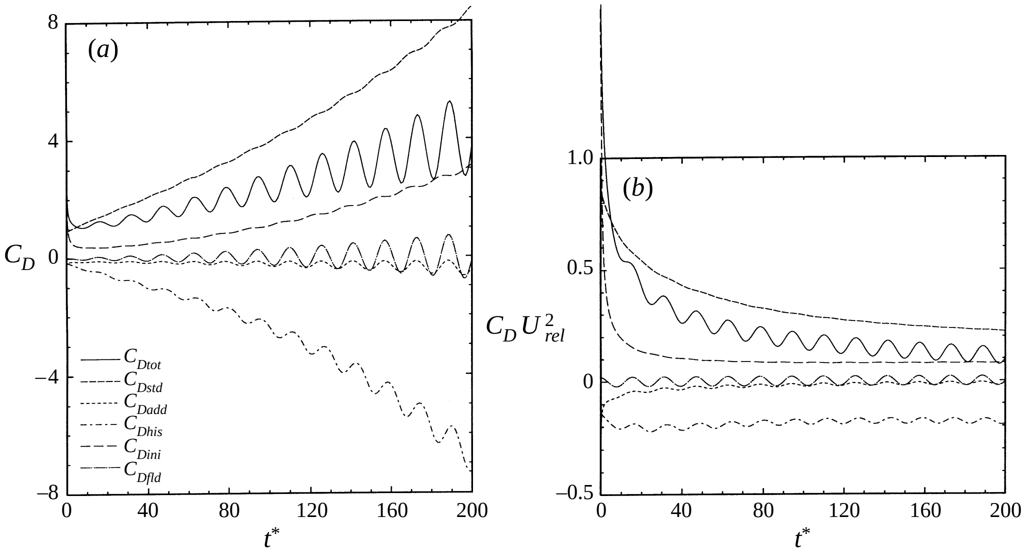

FIGURE 10. (a) C_{Dtot}, C_{Dstd}, C_{Dadd}, C_{Dhis}, C_{Dini}, and C_{Dfld} as a function of time obtained from the new equation for the same parameters as used in figure 9. (b) As (a) but the drag coefficients are multiplied by U^2_{rel}.

Again, the new equation (3.9a) produces very good agreement with the Navier–Stokes equations.

Figure 10(a) shows the temporal development of C_{Dtot}, C_{Dstd}, C_{Dadd}, C_{Dhis}, C_{Dini}, and C_{Dfld} obtained from the new equation for the same conditions used in figure 9. By comparing figures 8(a) and 10(a), we note that C_{Dfld} is strongly affected by and nearly proportional to the magnitude of the dimensionless frequency. This can be also found via a process of non-dimensionalization, which will be shown later in this section.

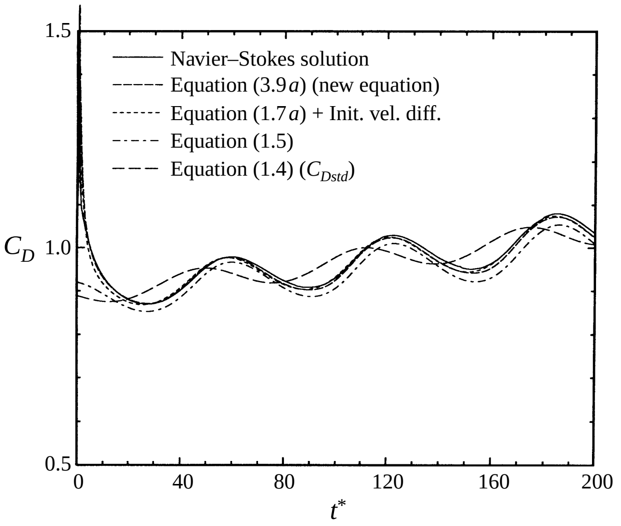

FIGURE 11. Drag coefficients as a function of time obtained from various equations for $Re_{to} = 150$ and $\rho_r = 200$ with the base flow oscillating with $Sl_\omega = 0.1$ and $\alpha_1 = 0.06$.

Figure 10(*b*) shows the temporal behaviour of the same drag coefficients as in figure 10(*a*) multiplied by U_{rel}^2, and thus represents the actual forces on the sphere.

Figure 11 plots the drag coefficients of the sphere as a function of time ($0 \leqslant t^* \leqslant 200$) for $Re_{to} = 150$ and $\rho_r = 200$ with the base flow oscillating with $Sl_\omega = 0.1$ and $\alpha_1 = 0.06$. The drag coefficients were obtained by solving the same five different equations as in figure 7. At $t^* = 200$, the particle Reynolds number becomes 115.6. Solutions from both (1.7*a*) and (3.9*a*) agree well with the Navier–Stokes solution. The improved performance of (1.7*a*) for the case of higher density ratio is due to the small acceleration number M_{A1} in the case of higher density ratio as will be shown in figure 17(*a*).

The contributions to the total drag coefficient from each term of the new equation are shown in figure 12 for the same conditions as figure 11. C_{Dadd}, C_{Dhis}, C_{Dini}, and C_{Dfld} are small compared to C_{Dstd} except the large C_{Dini} for a short initial period. The magnitude of the relative velocity U_{rel} is reduced slowly as will be seen in figure 17(*b*).

In order to examine the effect of each term in the new equation, we plot in figure 13 the drag coefficients as a function of time from the complete new equation (3.9*a*), without the history term, without the history and fluid acceleration terms, and with only C_{Dstd}. Neglecting the history term and the other terms in equation (3.9*a*) causes a small phase lag in the drag coefficient.

Figure 14 presents the temporal development of the drag coefficients ($0 \leqslant t^* \leqslant 200$) for the same conditions as used in figure 11 except $Sl_\omega = 0.4$. At $t^* = 200$, the particle Reynolds number becomes 103.2. Solutions from equations (1.7*a*) and (3.9*a*) agree well with the Navier–Stokes solution. Equation (1.4) predicts much smaller amplitude in the drag coefficient than do the others.

The contributions to the total drag coefficient from each term of the new equation are shown in figure 15 for the same conditions as used in figure 14. By comparing figures 12 and 15, we note that C_{Dfld} is strongly affected by the magnitude of the frequency, and its amplitude is almost linearly proportional to that of the frequency. Figure 16 displays the temporal behaviour of the drag coefficients from the complete new equation, without the history term, without the history and fluid acceleration

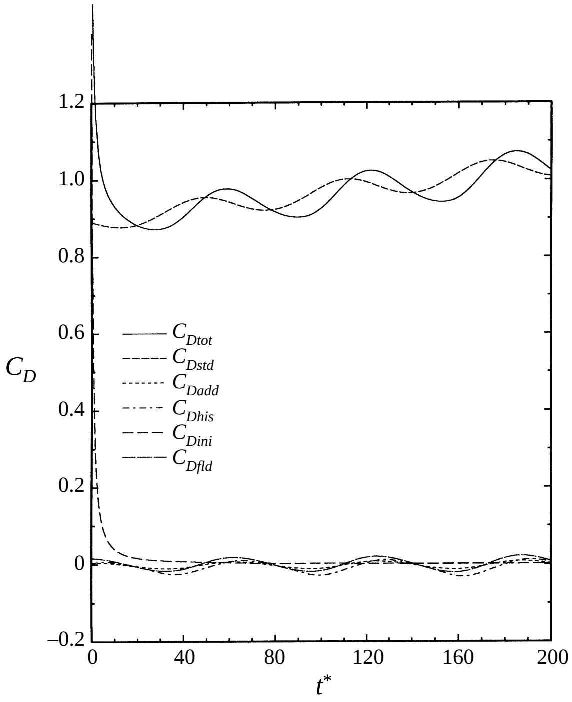

FIGURE 12. C_{Dtot}, C_{Dstd}, C_{Dadd}, C_{Dhis}, C_{Dini}, and C_{Dfld} as a function of time obtained from the new equation for the same parameters as used in figure 11.

terms, and with only C_{Dstd}. It is observed that neglecting the term C_{Dfld} causes the amplitude of the drag coefficient to be smaller.

Figure 17(*a*) shows the acceleration number M_{A1} as a function of time for four different cases: (i) $\rho_r = 5$, $Sl_\omega = 0.4$ and $\alpha_1 = 0.02$, (ii) $\rho_r = 5$, $Sl_\omega = 0.1$ and $\alpha_1 = 0.02$, (iii) $\rho_r = 200$, $Sl_\omega = 0.4$ and $\alpha_1 = 0.06$, and (iv) $\rho_r = 200$, $Sl_\omega = 0.1$ and $\alpha_1 = 0.06$. It is noted from the figure that although α_1 and Sl_ω are varied by less than an order of magnitude, the acceleration number (which is the primitive parameter) is varied by more than one order of magnitude. $[M_{A1}]_{av}$, the mean of M_{A1}, decreases as the density ratio increases, a similar behaviour to that of M_{A1} in figure 6(*a*), where $[M_{A1}]_{av}$ is defined by

$$\int_0^{t_f} [M_{A1}]_{av}(t)\,\mathrm{d}t = \left| \int_0^{t_f} \frac{2a}{|u-v|^2} \frac{\mathrm{d}|u-v|}{\mathrm{d}t} \mathrm{d}t \right| . \tag{3.13}$$

It is observed by inspection that $[M_{A1}]_{av}$ is not affected strongly by the magnitude of the dimensionless frequency at least for a simple harmonic oscillation (i.e. one Fourier mode) of the base flow. It will be shown later that the integrand of the right-hand side of equation (3.13) is a part of the integrand of the history integral. Also, the comparison of figures 13 and 16 indicates that the contribution from the history integral to the total drag is not increased when the frequency increases by a factor of 4.

Figure 17(*b*) shows the dimensionless relative velocity $U_{rel} = |u-v|/v_o$ as a function of time for the same cases as figure 17(*a*). This figure indicates, as expected, that U_{rel} for $\rho_r = 5$ decays faster than that for $\rho_r = 200$. Therefore, the history integral for the

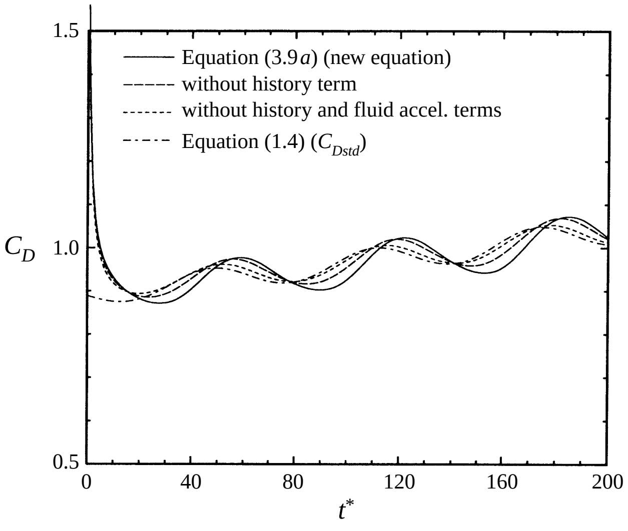

FIGURE 13. Drag coefficients as a function of time from the complete new equation, without the history term, without the history and fluid acceleration terms, and with only C_{Dstd} for the same parameters as used in figure 11.

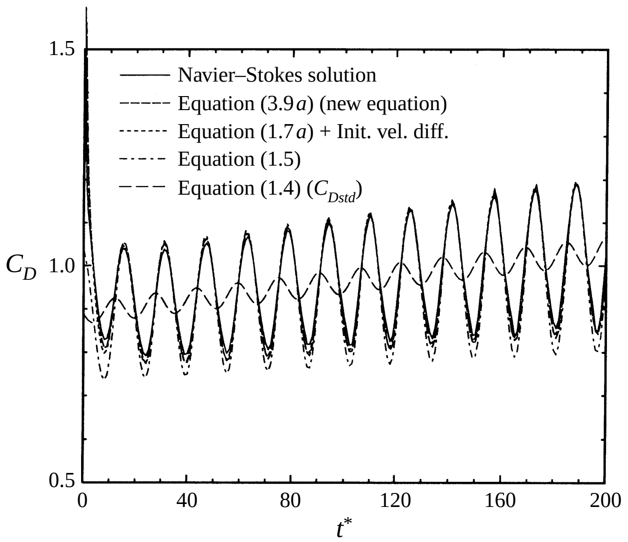

FIGURE 14. Drag coefficients as a function of time obtained from various equations for $Re_{to} = 150$ and $\rho_r = 200$ with the base flow oscillating with $Sl_\omega = 0.4$ and $\alpha_1 = 0.06$.

case of $\rho_r = 5$ is much larger than that for the case of $\rho_r = 200$ as indicated in the previous figures 8(*a*), 10(*a*), 12, and 15.

Finally, in order to examine the relative importance of the terms in equation (3.9*a*), we re-write it as

$$\frac{\mathrm{d}v}{\mathrm{d}t} = \frac{3}{8a}\frac{|u-v|(u-v)}{\rho_r}(C_{Dstd} + C_{Dadd} + C_{Dfld} + C_{Dhis} + C_{Dini} + C_{Dgrv}). \qquad (3.14)$$

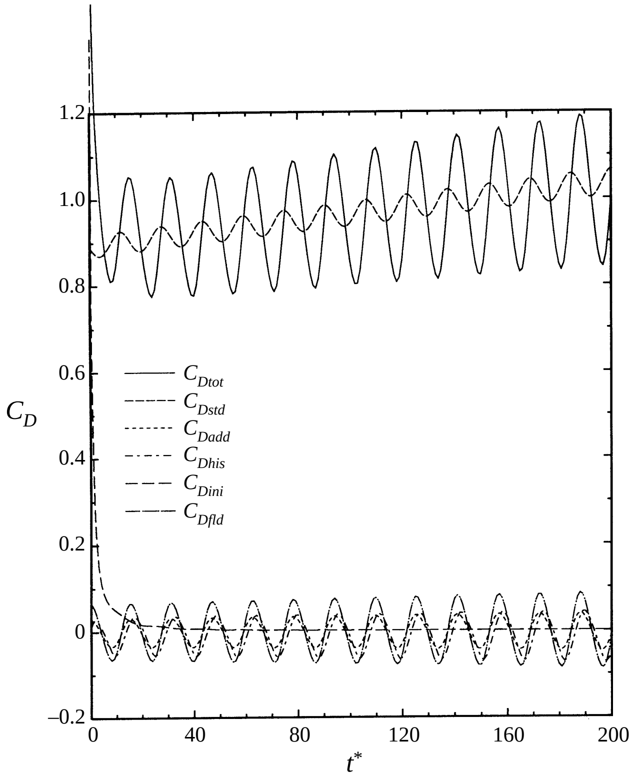

FIGURE 15. C_{Dtot}, C_{Dstd}, C_{Dadd}, C_{Dhis}, C_{Dini}, and C_{Dfld} as a function of time obtained from the new equation for the same parameters as used in figure 14.

The six terms on the right-hand side of equation (3.14) can be expressed as

$$C_{Dadd} = \frac{4}{3}\frac{a}{\mid u-v \mid (u-v)}\left(\frac{\mathrm{D}u}{\mathrm{D}t}-\frac{\mathrm{d}v}{\mathrm{d}t}\right) \approx \frac{4}{3}\frac{a}{(u-v)^2}\frac{\mathrm{d}\mid u-v \mid}{\mathrm{d}t} \approx \tfrac{2}{3}M_{A1}; \qquad (3.15)$$

$$C_{Dfld} = \frac{8}{3}\frac{a}{\mid u-v \mid (u-v)}\frac{\mathrm{D}u}{\mathrm{D}t} \approx \frac{8}{3}\frac{Sl_\omega}{\mid u^*-v^* \mid (u^*-v^*)}\frac{\partial u^*}{\partial t'}, \qquad (3.16)$$

where t' is the time normalized by frequency ω, and u^* and v^* the velocity normalized by the sphere injection velocity v_o;

$$\begin{aligned} C_{Dhis} &= \frac{12}{(\pi Re_R)^{1/2}|u^*-v^*|^2}\int_0^{t^*} K^*(t^*-\tau^*,\tau^*)\frac{\mathrm{d}|u^*-v^*|}{\mathrm{d}\tau^*}\,\mathrm{d}\tau^* \\ &\approx \frac{12}{(\pi Re_R)^{1/2}}\int_0^{t^*}\frac{K^*(t^*-\tau^*,\tau^*)}{|u^*-v^*|^2}\frac{\mathrm{d}|u^*-v^*|}{\mathrm{d}\tau^*}\,\mathrm{d}\tau^* \quad \text{if} \quad \frac{\mathrm{d}|u^*-v^*|^2}{\mathrm{d}t^*} \ll 1 \\ &\approx \frac{6}{(\pi Re_R)^{1/2}}\int_0^{t^*} K^*(t^*-\tau^*,\tau^*)\,S\,M_{A1}(\tau^*)\,\mathrm{d}\tau^* \qquad (3.17) \end{aligned}$$

with the integral kernel $K^*(t^*-\tau^*,\tau^*)$ given by

$$K^*(t^*-\tau^*,\tau^*) = \left\{(t^*-\tau^*)^{1/5} + G(\tau^*)\left[\frac{\pi^{1/2}}{2}Re_R^{3/2}\frac{|u^*(\tau^*)-v^*(\tau^*)|^3}{av_f f_H^3(Re_t)}(t^*-\tau^*)^2\right]^{2/5}\right\}^{-5/2},$$

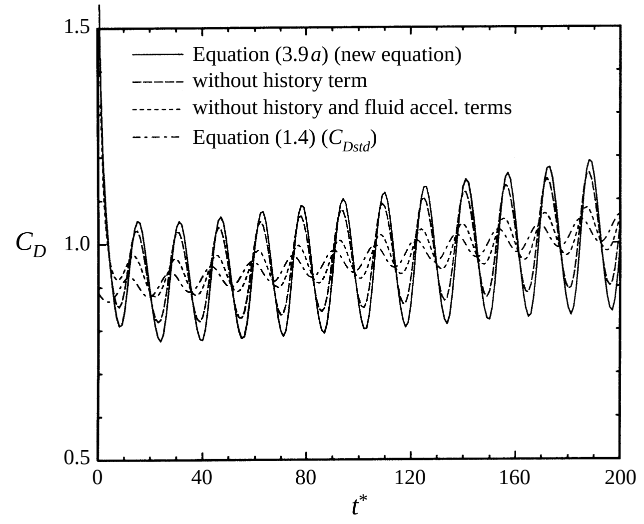

FIGURE 16. Drag coefficients as a function of time from the complete new equation, without the history term, without the history and fluid acceleration terms, and with only C_{Dstd} for the same parameters as used in figure 14.

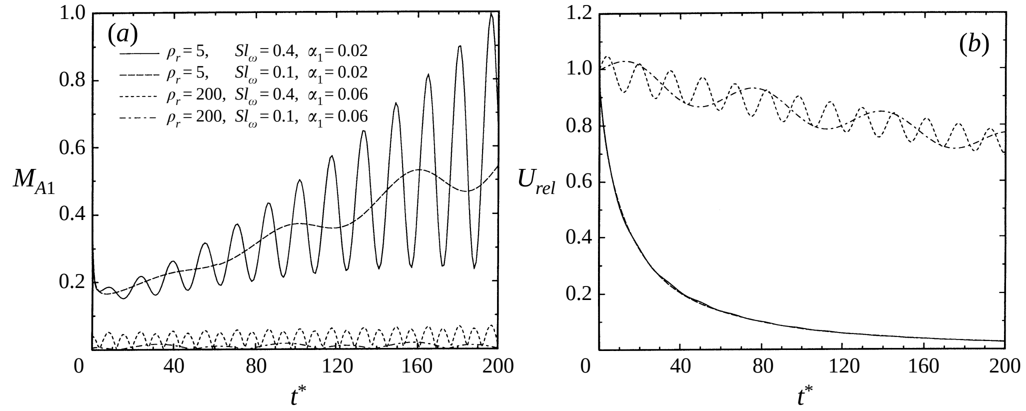

FIGURE 17. (a) Dimensionless relative acceleration M_{A1} and (b) dimensionless relative velocity U_{rel} as a function of time for four different cases.

where $Re_R = U_c a/\nu_f$, $S = \mathrm{sgn}(\mathrm{d}|u^* - v^*|/\mathrm{d}\tau^*)$, and t^* and τ^* are the times normalized by the convection time a/v_o;

$$C_{Dini} = \frac{12}{(\pi Re_R)^{1/2}} \frac{K_1^*(t^*)}{|u^* - v^*|(u^* - v^*)} [u^*(0) - v^*(0)] \tag{3.18}$$

where $K_1^*(t^*)$ is obtained from $K^*(t^*, \tau^* = 0)$ but with $G(\tau^*)$ replaced by G_1 (equation (3.9g));

$$C_{Dgrv} = \frac{8}{3} \frac{a(\rho_r - 1)g}{|u - v|(u - v)}. \tag{3.19}$$

Equations (3.15) and (3.17) show that C_{Dadd} and C_{Dhis} can be neglected compared to the quasi-steady drag C_{Dstd} when $M_{A1}(t) \ll C_{Dstd}(t)$ for all t. In fact, $M_{A1} \rightarrow 0$ produces the quasi-steady limit. Also, equation (3.17) indicates that C_{Dhis} is proportional to

$Re_R^{-1/2}$. Equation (3.16) shows that C_{Dfld} can be neglected compared to C_{Dstd} when Sl_ω is small. As mentioned before, the function K_1' in equation (3.18) contains G_1 which is explicitly a function of the density ratio ρ_r (see equation (3.9*g*)). As the density ratio becomes large, G_1 approaches unity, and the function $K_1'(t)$ becomes proportional to $1/t^2$ at large time. Thus, as the density ratio increases, the drag due to the initial velocity difference decays faster with time and would be negligible compared to C_{Dstd}.

3.5. *Flow structure*

In this subsection, we examine the physical processes of the unsteady, axisymmetric flow around a freely moving sphere injected into an initially stagnant fluid. The sphere will be decelerating due to the drag. All the figures in this subsection describe the flow around a sphere as a function of time ($0 \leqslant t^* \leqslant 300$) with the initial particle Reynolds number $Re_{to} = 150$, where $t^* = tv(0)/a$ and $Re_{to} = |u(0) - v(0)|2a/\nu_f$. The ratio of the sphere density to that of the fluid is $\rho_r = 5$. A grid with 121×121 mesh points is used with a computational domain extending in the downstream direction 121 sphere radii for better resolution of the wake region.

Figure 18 compares the streamlines of the unsteady flow (left-hand column) and steady flow (right-hand column) over a sphere at the same Reynolds numbers. The left-hand column figures 18*a–f* show the streamlines around the sphere at $t = 5$, 20, 40, 100, 200, and 300, respectively. The corresponding instantaneous Reynolds numbers are $Re_t = 96.6$, 53.8, 31.5, 11.2, 4.04, and 2.12, respectively. The dimensionless stream function ψ^* is defined in spherical coordinates via

$$W_\theta^* = \frac{v}{v_o} \frac{1}{r^* \sin\theta} \frac{\partial \psi^*}{\partial r^*}. \tag{3.20}$$

The stream function is normalized by va^2 where v is the instantaneous velocity of the sphere. On the other hand, the velocity W_θ^* is normalized by v_o, the initial injection velocity of the sphere (see § 2.2). For left- and right-hand columns the contour values of the stream function outside the recirculation zone are 0, 0.125, 0.5, 1.125, and 2, and those inside that zone are −0.02, −0.1, −0.25, −0.5, and −0.8.

As expected, the steady flow figures show that the size of the recirculation eddy decreases as Reynolds number decreases. On the other hand, the unsteady flow figures show that as the sphere decelerates, the eddy size grows monotonically even though the instantaneous Reynolds number of the sphere decreases. At $t = 300$, the size of the eddy becomes much larger than the sphere size; the length of the eddy is 15.4 radii measured from the centre of the sphere. This length is more than twice that of the eddy (6.8 radii) for the steady flow at $Re = 5000$ computed by Fornberg (1988) who solved numerically the steady stream function–vorticity equations. Note that the real flow past a sphere would not be steady at $Re = 5000$.

For a steady free stream relative to a sphere, the flow along the edge of the boundary layer on the sphere surface accelerates from the front stagnation point and reaches a maximum velocity at a location on the sphere surface that subtends an angle, θ_{st}, less than 90° (measured from the front stagnation point) and then starts to decelerate. The angle θ_{st} depends on Reynolds number. For an unsteady decelerating free stream, the flow along the boundary layer edge begins to decelerate at a location on the sphere surface with an angle smaller than θ_{st} at the same Reynolds number. This behaviour is evident in the shear stress distributions around the sphere shown in figure 19*a–f*. As a consequence, the free-stream deceleration reduces the angle of inception of the adverse pressure gradient along the surface compared to that for

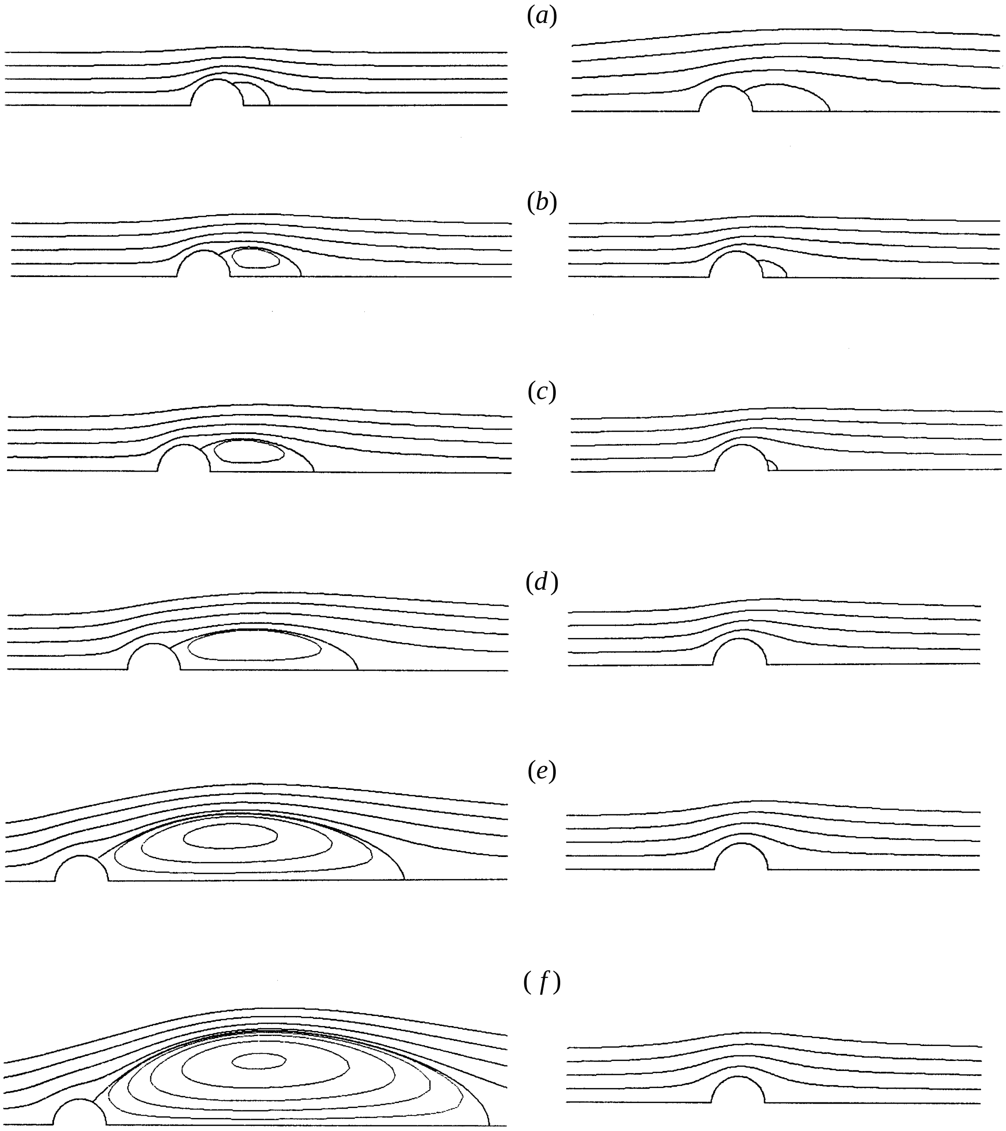

FIGURE 18. Streamlines of the unsteady flow around a decelerating sphere (left-hand column) at (*a*) $t = 5$, (*b*) 20, (*c*) 40, (*d*) 100, (*e*) 200, and (*f*) 300 for $Re_{to} = 150$ and $\rho_r = 5$ with the corresponding instantaneous Reynolds numbers (*a*) $Re_t = 96.6$, (*b*) 53.8, (*c*) 31.5, (*d*) 11.2, (*e*) 4.04, and (*f*) 2.12, respectively; streamlines of the steady flow (right-hand column) at the same Reynolds numbers as those of the unsteady flow in the left-hand column.

the steady flow at the same Reynolds number as shown in figure 19*a*–*f*. Accordingly, the free-stream deceleration reduces the separation angle θ_s compared to that for a steady flow at the same Reynolds number. Note that the separation angle is that at which the shear stress vanishes at the sphere surface. Figure 18 (also figure 19) shows that for the steady flow, the location of separation on the sphere surface moves toward the rear stagnation point with the reduction of Reynolds number. By contrast, the separation location for the decelerating sphere does not change significantly.

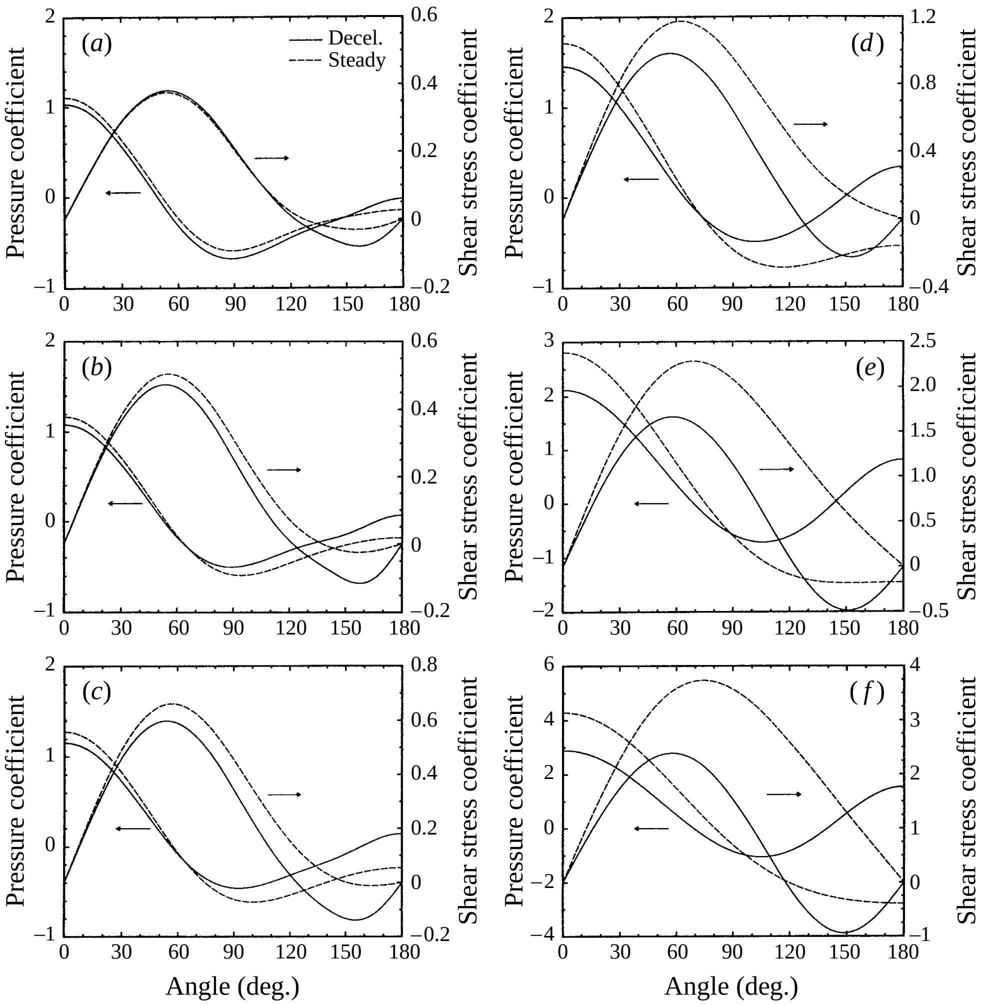

Figure 19. Pressure and shear stress coefficients around the decelerating sphere surface at the same times as those in figure 18, and at steady state at the same Reynolds numbers.

At the time of injecting the sphere into the fluid with the initial parameters described at the first paragraph of this subsection, there is no flow separation (i.e. $\theta_s = 180°$). This angle decreases rapidly to 121° at $t = 11$ during the initial flow development around the sphere due to its sudden injection into the fluid. After this transition, the separation angle increases slowly to 126° at $t = 104$, and then decreases monotonically to 118° at $t = 300$. Because the separation location (actually the separation circle around the sphere) is not fixed but moves as a function of time, the fluid particles flowing in the boundary layer on the sphere surface are constantly trapped in the recirculation eddy. In addition, it should be noted that as a new wake is generated behind the decelerating sphere, it moves downstream with a velocity smaller than that of the wake generated earlier. Therefore, the size of the recirculation eddy grows as the sphere decelerates. Note that when a sphere experiences a higher deceleration rate than that of the present study, the location of separation would move more rapidly to the front stagnation point. This was reported by Chang & Maxey (1995) for constant

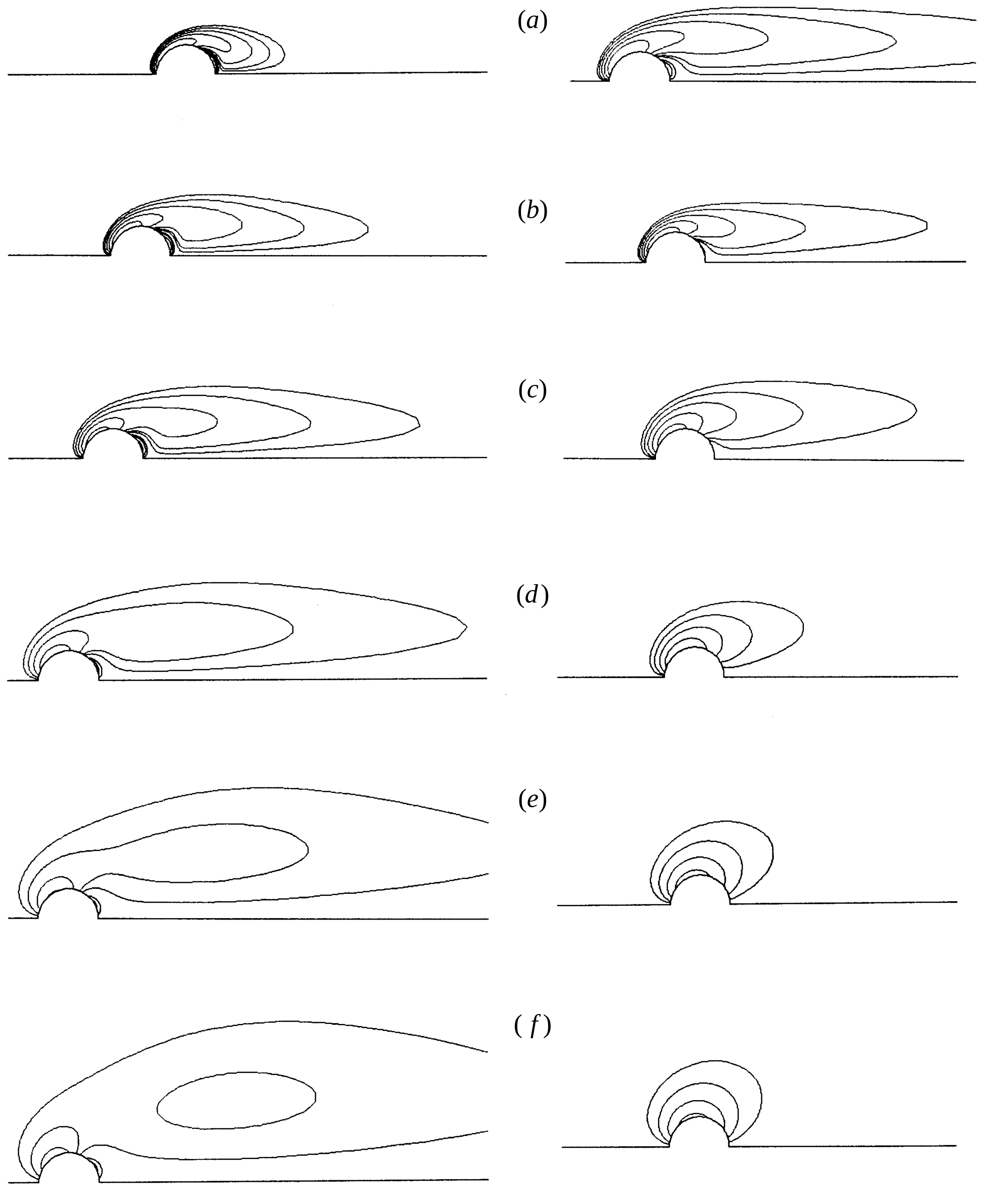

FIGURE 20. Vorticity contours of the unsteady flow around a decelerating sphere (left-hand column) at the same times as those in figure 18; vorticity contours of the steady flow (right-hand column) at the same Reynolds numbers as those of figures in the left-hand column.

M_{A1} (= 1 or 2). They performed a numerical simulation for linearly decelerating flows (constant M_{A1}) past a fixed sphere for $0.1 \leqslant Re \leqslant 20$.

It is interesting that the adverse pressure gradient at the sphere surface for the case of a decelerating sphere occurs even at small Reynolds numbers for which the steady flow shows no separation (see figure 19*e*, *f*). Thus, the recirculation eddy exists at small Reynolds numbers for the case of a decelerating sphere. A similar phenomenon has been also reported by Chang & Maxey (1995) where the size of the recirculation eddy was comparable with the sphere size. It is also seen from figure 18 that the steady flow fore-aft symmetry is enhanced as Reynolds number decreases, whereas the unsteady decelerating flow becomes more asymmetric because the size of the recirculation eddy grows continuously.

The left-hand column of figure 20(*a*–*f*) shows the vorticity contours around the sphere at the same times (and the same instantaneous Reynolds numbers) as those in figures 18 and 19. The vorticity used in these figures is normalized by (v/a) where v is the instantaneous velocity of the sphere. The negative contour values of the vorticity are -3.2, -1.6, -0.8, -0.4 and -0.2, and the positive values with the highest magnitude at the sphere surface are 0.8, 0.4 and 0.2. The vorticity associated with counterclockwise rotation is assumed positive. The right-hand column of figure 20(*a*–*f*) shows the vorticity contours at steady state for the same contour values and at the same Reynolds numbers as those of figures in the left-hand column.

The right-hand column of figure 20(*a*–*f*) shows that for the steady flow past a sphere, the vorticity becomes more uniformly distributed around the sphere as Reynolds number decreases because of the enhanced role of momentum diffusion as Reynolds number decreases. On the other hand, the left-hand column figure of 20(*a*–*f*) indicates that as the sphere decelerates, vorticity is being continuously advected farther downstream even though the instantaneous Reynolds number of the sphere is becoming smaller. The reason is that the fluid particles are being constantly trapped in the recirculation eddy, and thus the size of the recirculation eddy grows as the sphere decelerates as discussed above. At $t = 300$, the vorticity contour of -0.4 is divided into two parts, and a centre of vorticity concentration appears downstream. A similar phenomenon was also reported by Chang & Maxey (1995) at some time after the free-stream deceleration (from Reynolds number 10 to 1) stops.

Figures 19 displays the pressure and shear stress coefficients around the sphere surface at the same times (and the same instantaneous Reynolds numbers) as those in figures 18 and 20 and also shows those at steady state at the same Reynolds numbers. The pressure coefficient and the shear stress coefficient are defined as $2(p-p_\infty)/\rho v^2$ and $2\tau_{r\theta}/\rho v^2$, respectively, where v is the instantaneous velocity of the sphere. Comparing the decelerating flow with the steady flow at the same Reynolds number, it is seen that for the decelerating flow: (i) the front stagnation pressure is lower than that of the steady state, (ii) the angle of inception of the adverse pressure gradient on the sphere surface is smaller than that for the steady flow, (iii) the rear stagnation pressure is higher than that for the steady state, and (iv) the shear stress around the sphere is lower than that for the steady state. These are the reasons why the unsteady drag for a decelerating sphere is lower than the drag for the steady state at the same Reynolds number.

4. Conclusion

A new equation for the rectilinear motion of a spherical particle has been proposed. It includes a modified history term and a drag force due to the initial velocity difference between the particle and the carrier flow (equation (3.9*a*)). Comparison with the numerical solution of the Navier–Stokes equations shows that the new equation (3.9*a*) provides a more accurate prediction of the particle motion than any other equation developed to date over particle Reynolds number in the range of 2 to 150 and particle to fluid density ratio in the range of 5 to 200.

The modified history term in the new equation recovers the Basset history term for large acceleration number M_{A1} and recovers the term proposed by MA for low acceleration number.

	History force		Total drag	
Time	Present equation	LB	LB	Present equation
0.2	0.258	0.264	1.280 94	1.275 60
0.3	0.206	0.212	1.229 21	1.223 25
0.4	0.174	0.181	1.198 41	1.192 03
0.5	0.153	0.160	1.177 41	1.170 73
1	0.100	0.108	1.125 42	1.118 03
10	0.177×10^{-1}	0.241×10^{-1}	1.041 16	1.035 49
100	0.125×10^{-2}	0.215×10^{-2}	1.019 22	1.018 99
400	0.147×10^{-3}	0.187×10^{-3}	1.017 25	1.017 89
600	0.738×10^{-4}	0.833×10^{-4}	1.017 15	1.017 81
800	0.447×10^{-4}	0.469×10^{-4}	1.017 11	1.017 78
900	0.363×10^{-4}	0.370×10^{-4}	1.017 10	1.017 78
1000	0.301×10^{-4}	0.300×10^{-4}	1.017 09	1.017 77

TABLE 2. Comparison of the temporal behaviour of the history force and total drag obtained from the present equation and those of Lovalenti & Brady (1993, 1995) and Sano (1981) for a sphere with impulsive start from rest to $Re = 0.1$. The forces are normalized by the steady Stokes drag $(6\pi a\mu U_2)$.

It is found that the steady flow fore-aft symmetry is enhanced as Reynolds number decreases, whereas the unsteady decelerating flow becomes more asymmetric because the size of the recirculation eddy grows continuously.

This work has been supported by the Air Force Office of Scientific Research under grant No. F49620-93-1-0028 with Dr Julian Tishkoff acting as the technical monitor. We would like to thank the reviewer who commented on the $-\infty$ lower limit of the history integral. The support of the San Diego Supercomputer Center directly and the San Diego Supercomputer Center under a block grant of the Office of Academic Computing of UCI are gratefully appreciated.

Appendix. Behaviour of the proposed particle motion equation for low Reynolds number ($Re < 1$)

We compare the history force and total drag of our proposed equation with those of Lovalenti & Brady (1993*a*, *b*, 1995) for a sphere with impulsive start from rest ($U_1 = 0$) to a small Reynolds number ($Re = 2aU_2/\nu = 0.1$) for which the expression of Lovalenti & Brady (1993*a*, *b*, 1995) reduces to that of Sano (1981). The comparison is shown in table 2. The expression of Lovalenti & Brady is denoted as LB. Table 2 shows that the results from the present equation compare favourably with those from Lovalenti & Brady and Sano. The difference between our results and those of LB is always less than 1% of the total drag force and asymptotically goes to zero for long time. As a percentage of the maximum history force, the disagreement never exceeds 3%. The instantaneous percentage disagreement is less than 8% for $t \leqslant 1$, peaks at about 42% for $t = 100$, and then asymptotically diminishes to zero for long time. The peak in the discrepancy, however, occurs after the history force is truly negligible and inconsequential.

Now, for the case where $U_1 > 0$, we can make comparisons with both LB and Lawrence & Mei (1995), denoted as LM, for two parameter cases. These results are

		$K(t)$			Total drag		
	Time	Present equation	LB	LM	Present equation	LB	LM
(*a*)	0.100	0.592	0.666	0.85	1.4421	1.5002	1.6141
	0.178	0.417	0.481	0.53	1.3255	1.3769	1.4008
	0.316	0.288	0.343	0.34	1.2395	1.2849	1.2741
	0.562	0.193	0.240	0.25	1.1761	1.2162	1.2141
	1.00	0.124	0.164	0.17	1.1301	1.1656	1.1608
	1.78	0.759×10^{-1}	0.108	0.12	1.0981	1.1282	1.1275
	3.16	0.440×10^{-1}	0.679×10^{-1}	0.7×10^{-1}	1.0768	1.1015	1.0941
	5.62	0.238×10^{-1}	0.396×10^{-1}	0.4×10^{-1}	1.0633	1.0826	1.0741
	10.0	0.120×10^{-1}	0.208×10^{-1}	0.2×10^{-1}	1.0555	1.0701	1.0608
	17.8	0.561×10^{-2}	0.927×10^{-2}	0.1×10^{-1}	1.0512	1.0624	1.0541
	31.6	0.245×10^{-2}	0.323×10^{-2}	0.37×10^{-2}	1.0491	1.0584	1.0499
	56.2	0.998×10^{-3}	0.778×10^{-3}	0.9×10^{-3}	1.0481	1.0568	1.0481
	100	0.384×10^{-3}	0.121×10^{-3}	0.14×10^{-3}	1.0477	1.0563	1.0476
	178	0.141×10^{-3}	0.198×10^{-4}	0.21×10^{-4}	1.0476	1.0563	1.0475
	300	0.548×10^{-4}	0.626×10^{-5}	0.65×10^{-5}	1.0475	1.0563	1.0475
	1000	0.574×10^{-5}	0.563×10^{-6}	0.56×10^{-6}	1.0475	1.0563	1.0475
(*b*)	0.316	0.347	0.596	0.5	1.2009	1.3067	1.2315
	0.562	0.204	0.379	0.38	1.1723	1.2633	1.2075
	1.00	0.112	0.227	0.21	1.1539	1.2329	1.1735
	1.78	0.575×10^{-1}	0.125	0.13	1.1430	1.2125	1.1575
	3.16	0.274×10^{-1}	0.611×10^{-1}	0.6×10^{-1}	1.1370	1.1997	1.1435
	5.62	0.121×10^{-1}	0.252×10^{-1}	0.27×10^{-1}	1.1339	1.1925	1.1369
	10.0	0.502×10^{-2}	0.843×10^{-2}	0.85×10^{-2}	1.1325	1.1892	1.1332
	17.8	0.196×10^{-2}	0.229×10^{-2}	0.27×10^{-2}	1.1319	1.1880	1.1320
	31.6	0.728×10^{-3}	0.599×10^{-3}	0.61×10^{-3}	1.1316	1.1876	1.1316
	56.2	0.259×10^{-3}	0.178×10^{-3}	0.18×10^{-3}	1.1316	1.1875	1.1315
	100	0.895×10^{-4}	0.563×10^{-4}	0.50×10^{-4}	1.1315	1.1875	1.1315
	178	0.301×10^{-4}	0.178×10^{-4}	0.16×10^{-4}	1.1315	1.1875	1.1315
	300	0.111×10^{-4}	0.625×10^{-5}	0.50×10^{-5}	1.1315	1.1875	1.1315
	1000	0.106×10^{-5}	0.561×10^{-6}	0.40×10^{-6}	1.1315	1.1875	1.1315

TABLE 3. Comparison of the temporal behaviour of the history force and total drag obtained from the present equation and those of Lovalenti & Brady (1993, 1995) and Lawrence & Mei (1995) for a sphere making a step change of its velocity at $t = 0$ (*a*) from $Re_1 = 0.1$ to $Re_2 = 0.3$ and (*b*) from $Re_1 = 0.8$ to $Re_2 = 1.0$. $K(t)$ is listed. The history force normalized by the steady Stokes drag equals the product of $K(t)$ and $(1 - U_1/U_2)$.

shown in table 3. The comparison with LB is not as good here as it was with the $U_1 = 0$ cases. However, the LB and LM comparisons were not totally satisfactory either. Our results for the history force differ from the LM results by as much as 30% of the maximum value of the history force. The LB results are generally closer to the LM results but do differ by as much as 22% of the maximum history force. Our maximum disagreement however is about 10% of the total drag force for the case of $Re_1 = 0.1$ and $Re_2 = 0.3$ and is about 2% of the total drag force for the case of $Re_1 = 0.8$ and $Re_2 = 1$.

In summary, while there is some disagreement with the theories (outside the designed range for our equation), it is not a significant factor in the total drag force.

REFERENCES

Basset, A. B. 1888 *A Treatise on Hydrodynamics*, vol. 2, p. 285. Dover.

Berezin, I. S. & Zhidkov, N. P. 1965 *Computing Methods*, p. 299. Addison-Wesley.

Berlemont, A., Desjonqueres, P. & Gouesbet, G. 1990 Particle Lagrangian simulation in turbulent flows. *Intl. J. Multiphase Flow* **16**, 19–34.

Boussinesq, J. 1903 *Theorie Analytique de la Chaleur* (L'École Polytechnique, Paris), vol. 2, p. 224.

Chang, E. J. & Maxey, M. R. 1994 Accelerated motion of rigid spheres in unsteady flow at low to moderate Reynolds numbers. Part 1. Oscillatory motion. *J. Fluid Mech.* **277**, 347–379.

Chang, E. J. & Maxey, M. R. 1995 Unsteady flow about a sphere at low to moderate Reynolds numbers. Part 2. Accelerated motion. *J. Fluid Mech.* **303**, 133–153.

Chung, J. N. 1982 The motion of particles inside a droplet. *Trans. ASME* C: *J. Heat Transfer* **104**, 438–445.

Clift, R., Grace, J. R. & Weber, M. E. 1978 *Bubbles, Drops, and Particles.* Academic.

Fornberg, B. 1988 Steady viscous flow past a sphere at high Reynolds numbers. *J. Fluid Mech.* **190**, 471–489.

Kim, I., Elghobashi, S. & Sirignano, W. A. 1993 Three-dimensional flow over two spheres placed side by side. *J. Fluid Mech.* **246**, 465–488.

Kim, I., Elghobashi, S. & Sirignano, W. A. 1995 Unsteady flow interactions between an advected cylindrical vortex tube and a spherical particle. *J. Fluid Mech.* **288**, 123–155.

Kim, I., Elghobashi, S. & Sirignano, W. A. 1996 The motion of a spherical particle in unsteady flows at moderate Reynolds numbers. *AIAA Paper* 96-0081.

Kim, I., Elghobashi, S. & Sirignano, W. A. 1997 Unsteady flow interactions between a pair of advected vortex tubes and a rigid sphere. *Intl J. Multiphase Flow* **23**, 1–23.

Lawrence, C. J. & Mei, R. 1995 Long-time behaviour of the drag on a body in impulsive motion. *J. Fluid Mech.* **283**, 307–327.

Lovalenti, P. M. & Brady, J. F. 1993*a* The hydrodynamic force on a rigid particle undergoing arbitrary time-dependent motion at small Reynolds number. *J. Fluid Mech.* **256**, 561–605.

Lovalenti, P. M. & Brady, J. F. 1993*b* The force on a sphere in a uniform flow with small-amplitude oscillations at finite Reynolds number. *J. Fluid Mech.* **256**, 607–614.

Lovalenti, P. M. & Brady, J. F. 1995 The temporal behaviour of the hydrodynamic force on a body in response to an abrupt change in velocity at small but finite Reynolds number. *J. Fluid Mech.* **293**, 33–46.

Maxey, M. R. 1993 The equation of motion for a small rigid sphere in a nonuniform or unsteady flow. *Gas-Solid Flows.* ASME/FED, Vol. 166, pp. 57–62.

Maxey, M. R. & Riley, J. J. 1983 Equation of motion for a small rigid sphere in a nonuniform flow. *Phys. Fluids* **26**, 883–889.

Mei, R. 1994 Flow due to an oscillating sphere and an expression for unsteady drag on the sphere at finite Reynolds number. *J. Fluid Mech.* **270**, 133–174.

Mei, R. & Adrian, R. J. 1992 Flow past a sphere with an oscillation in the free-stream and unsteady drag at finite Reynolds number. *J. Fluid Mech.* **237**, 323–341 (referred to herein as MA).

Mei, R., Lawrence, C. J. & Adrian, R. J. 1991 Unsteady drag on a sphere at finite Reynolds number with small fluctuations in the free-stream velocity. *J. Fluid Mech.* **233**, 613–631.

Odar, F. 1966 Verification of the proposed equation for calculation of the forces on a sphere accelerating in a viscous fluid. *J. Fluid Mech.* **25**, 591–592.

Odar, F. & Hamilton, W. S. 1964 Forces on a sphere accelerating in a viscous fluid. *J. Fluid Mech.* **18**, 302–314 (referred to herein as OH).

Oseen, C. W. 1927 *Hydrodynamik*. Leipzig: Akademische Verlagsgesellschaft.

Rivero, M., Magnaudet, J. & Fabre, J. 1991 Quelques resultants nouveaux concernant les forces exercees sur une inclusion spherique par en ecoulement accelere. *C.R. Acad. Sci. Paris* **312**(II), 1499–1506.

Sano, T. 1981 Unsteady flow past a sphere at low Reynolds number. *J. Fluid Mech.* **112**, 433–441.

Taneda, S. 1956 Experimental investigation of the wake behind a sphere at low Reynolds number. *J. Phys. Soc. Japan* **11** 1104–1108.

Vinokur, M. 1983 On one-dimensional stretching functions for finite-difference calculations. *J. Comput. Phys.* **50**, 215–234.